



POLITECNICO DI BARI

DEPARTMENT OF ELECTRICAL AND INFORMATION ENGINEERING
Master Degree in Telecommunication Engineering

Electromagnetic Security

Electromagnetic Security through Simulation and Analysis of EM Fields and Antenna Arrays

Students

Damato Anna Vittoria

Di Benedetto Raffaele

Nardone Antonio

Sbiroli Carolina

Contents

1 EMC Analysis of a Pair of Shielded and Unshielded Dipoles	2
1.1 Simulation Goals	2
1.2 Background	3
1.2.1 Radiated Emissions	3
Limits	5
1.2.2 Electromagnetic Shielding	6
1.3 Simulation Software and Setup	9
1.3.1 Model Configuration and Dipole Length Optimization	9
1.4 Two Dipoles Model	11
1.4.1 Model Configuration	11
1.4.2 Simulation	12
Common Mode Current	12
Differential Mode Current	12
1.4.3 Results	13
Common Mode Current	13
Differential Mode Current	14
1.5 Shield Box Model	15
1.5.1 Model Configurations	15
1.5.2 Simulation and Results	16
1.6 Shield Box with Aperture Model	17
1.6.1 Model Configurations	17
1.6.2 Simulation	18
1.6.3 Results	19
1.7 Conclusion	21
2 Design and Analysis of Microstrip Patch Antenna Arrays	23
2.1 Simulation Goals	23
2.2 Background	25
2.2.1 Patch Microstrip	25
2.2.2 Antenna Array	26
ULA Array	27
Binomial Array	29
Chebyshev Array	30
2.3 Simulation Software and Setup	32
2.3.1 Patch Microstrip Parameters Optimazation	32
2.4 ULA Array	35
2.4.1 Number of Antenna Sweep	35
Simulation	35
Results	37

2.4.2	Phase Shift Sweep	40
Simulation	40	
Results	42	
2.5	Binomial Array	46
2.5.1	Simulation	46
2.5.2	Results	47
2.6	Chebyshev Array	50
2.6.1	Simulation	50
2.6.2	Results	51
2.7	Comparison	55
2.8	Conclusion	59
	Bibliography	61

Chapter 1

EMC Analysis of a Pair of Shielded and Unshielded Dipoles

This project is part of the study of electromagnetic safety, with a focus on the behaviour and characteristics of shielded and unshielded dipole pairs. The study focuses on the design, optimisation and experimental analysis of these antennas, with the aim of understanding the implications on electromagnetic emissions and electromagnetic compatibility (EMC).

1.1 Simulation Goals

The main objectives of this chapter are:

- Optimisation of the length of a single dipole antenna to operate at the frequency of interest of 5 GHz , reducing the reflection coefficient (S_{11}) to ensure maximum power radiation and proper antenna matching. This was done through parametric sweeps of the dipole length to centre the minimum of S_{11} at 5 GHz ;
- Analysis of the radiated emission of a pair of dipoles excited in both common mode and differential mode at an operating frequency of 5 GHz . This includes obtaining 3D radiation patterns for both modes and evaluating the radiated electric field as a function of frequency at a distance of 10 metres;
- Comparison of the radiated emission levels obtained for the dipole pair (in common and differential mode) with the CISPR regulatory limits for Class A and B. This analysis aims to identify whether emissions exceed the permitted thresholds and under which conditions;
- Study and design a metal shield made in PEC (Perfect Electric Conductor) for the differential mode in order to reduce electromagnetic emissions below regulatory limits;
- Analysis of the impact of a square aperture in the screen on shielding performance. This includes varying the size of the aperture and evaluating the resulting radiated electric field as a function of aperture size at the 5 GHz frequency. The objective is to determine the optimal aperture size that will allow the shield to remain below emission limits.

1.2 Background

Before analysing radiated emissions, it is important to remember the radiative properties of an elementary (or Hertzian) dipole, the different limits imposed by CISPR and the FCC, and the shielding technique adopted to reduce emissions.

1.2.1 Radiated Emissions

An electric dipole can be modelled as an infinitesimal current element $I dl$ oriented along the z axis. The radiated field can be expressed in spherical coordinates (r, θ, ϕ) , with the radiation distributed in all directions. Analysing the magnetic field, we observe that the only non-zero component is H_ϕ , expressed as:

$$H_\phi = \frac{I dl}{4\pi} \sin \theta \left(\frac{j\beta}{r} + \frac{1}{r^2} \right) e^{-j\beta r} \quad (1.1)$$

while the electric field has the following components:

$$E_r = \eta \frac{Idl}{2\pi} \cos \theta \left(\frac{1}{r^2} + \frac{1}{j\beta r^3} \right) e^{-j\beta r}; \quad (1.2)$$

$$E_\theta = \eta \frac{Idl}{4\pi} \sin \theta \left(\frac{j\beta}{r} + \frac{1}{j\beta r^2} + \frac{1}{j\beta r^3} \right) e^{-j\beta r}; \quad (1.3)$$

where $\eta = \sqrt{\frac{\mu_0}{\epsilon_0}}$ represents the intrinsic impedance of the medium and $\beta = \frac{2\pi}{\lambda} = \omega \sqrt{\mu_0 \epsilon_0} = \frac{\omega}{c}$ is the propagation constant. When considering the far field condition ($r \gg \lambda$), the terms $\frac{1}{r^2}$ and $\frac{1}{r^3}$ can be neglected, simplifying the equations to the dominant terms:

$$H_\phi = \frac{Idl}{4\pi} \sin \theta \frac{j\beta}{r} e^{-j\beta r}; \quad (1.4)$$

$$E_\theta = \eta \frac{Idl}{4\pi} \cos \theta \frac{j\beta}{r} e^{-j\beta r}; \quad (1.5)$$

In this condition, the electric and magnetic fields are orthogonal to each other and perpendicular to the direction of propagation, assuming the typical behaviour of a plane wave. Furthermore, the Poynting vector, representing the electromagnetic power flow, is oriented in the radial direction r , and is purely real, indicating the presence of only active power.

The value of the electric field at point P is proportional to the dipole current, the inverse of the distance and an angular propagation factor, which can be expressed as:

$$\bar{E}(P) \propto I \frac{1}{r} \bar{f}(\theta, \phi) e^{-j\beta r} \quad (1.6)$$

where $\bar{f}(\theta, \phi)$ is the antenna factor, which describes the distribution of radiation in space. For a Hertzian dipole, it is given by $\sin \theta$, which implies that maximum radiation occurs in the normal direction with respect to the dipole axis, confirming the typical doughnut shape of the radiation pattern.

Radiated emissions from CM and DM currents

If we consider two cables, along the z -axis and aligned along the x -direction, which are arranged horizontally at a distance s from each other, we can model each cable as if it were a dipole. Let us assume that the following conditions apply:

- Farfield approximation;
- $s, L \ll d$.

where L is the length of the cables, s is the distance between them and d represents the distance of point P from the two cables.

The electromagnetic emissions radiated by a dipole system can be analysed by considering the common mode (CM) and differential mode (DM) currents. From now on, the objective will be to evaluate the maximum of radiation, which in the case of the dipole, having the antenna factor $\bar{F}(\theta, \phi) = \sin \theta$, lies at $\theta = \frac{\pi}{2}$ (plane xy).

In the case of CM currents, the two cables carry the same current in the same direction, and the total electric field results:

$$\bar{E}_{\text{tot}}(P) = j\mu_0 f L I_C \frac{e^{-j\beta r}}{r} \cos\left(\beta \frac{s}{2} \cos \phi\right) \quad (1.7)$$

If the distance between the wires is much less than the wavelength ($s \ll \lambda$), the argument of the cosine tends to 0, so $\cos\left(\beta \frac{s}{2} \cos \phi\right) \rightarrow 1$ allowing the field to be approximated as:

$$\bar{E}_{\text{tot}}(P) = j\mu_0 f L I_C \frac{e^{-j\beta r}}{r} \quad (1.8)$$

From this expression, we see that the emission is proportional to the frequency f , the cable length L and the common mode current I_C . Therefore, to reduce the emission, one can act on these parameters.

In the case of DM currents, the two cables carry currents of equal intensity but in opposite directions. The total electric field results:

$$\bar{E}_{\text{tot}}(P) = -\mu_0 f L I_D \frac{e^{-j\beta r}}{r} \sin\left(\beta \frac{s}{2} \cos \phi\right) \quad (1.9)$$

Again, if $s \ll \lambda$, the sine can be approximated to its argument, and the expression of the radiated electric field is:

$$\bar{E}_{\text{tot}}(P) = -\pi f^2 \mu_0 \sqrt{\mu_0 \epsilon_0} I_D L s \frac{e^{-j\beta r}}{r} \cos \phi \quad (1.10)$$

where $L \cdot s$ represents the area between the two cables. It is observed here that the electric field radiated by DM currents is proportional to the square of the frequency and the area between the two cables. To minimise differential mode emissions, it is therefore useful to reduce the distance between the cables s .

In conclusion, common mode emissions tend to be higher than differential mode emissions, and mitigation techniques should focus on reducing cable lengths, cable spacing and the use of appropriate shielding.

Limits

The study of electromagnetic compatibility (EMC) is motivated by the imposition of regulatory requirements governing the movement of products on the market. In Europe, the CE marking is required to sell a device, which guarantees compliance with EMC regulations. In the United States, the body responsible for regulating communications is the Federal Communications Commission (FCC), which defines the range of usable radio frequencies between 9 kHz and 3000 GHz . However, not all frequencies are used, as devices with different technologies and purposes only use certain portions of the spectrum.

In Europe, EMC regulations are issued by the International Special Committee on Radio Interference (CISPR), part of the International Electrotechnical Commission (IEC). CISPR has no legislative power, as it develops recommendations that are not mandatory, but whose adoption is strongly recommended to national governments. These regulations set maximum emission limits, both conducted and radiated, and distinguish two classes of devices:

- Class A: devices for industrial environments (represented by the dotted red line in Fig. 1.1 and 1.2);
- Class B: devices for residential environments (represented by the dotted green line in Fig. 1.1 and 1.2).

The limits for Class B are more restrictive than those for Class A, since in a residential environment it is more difficult to manage interference than in an industrial environment, where sources of interference can be more easily identified and mitigated. Radiated emissions are considered for frequencies above 30 MHz . Limits are defined over different distances: 3 m and 10 m . The farfield condition, in which an electromagnetic wave can be approximated as being plane, depends on the wavelength λ . To guarantee this approximation, the distance to the antenna must be at least 4 or 5 times the wavelength. The limits imposed by CISPR are shown in Fig. 1.1. As we can see, the substantial difference with the FCC limits in Fig. 1.2, apart from the levels being lower on average, is that the measurement is made in both cases at a distance of 10 metres.

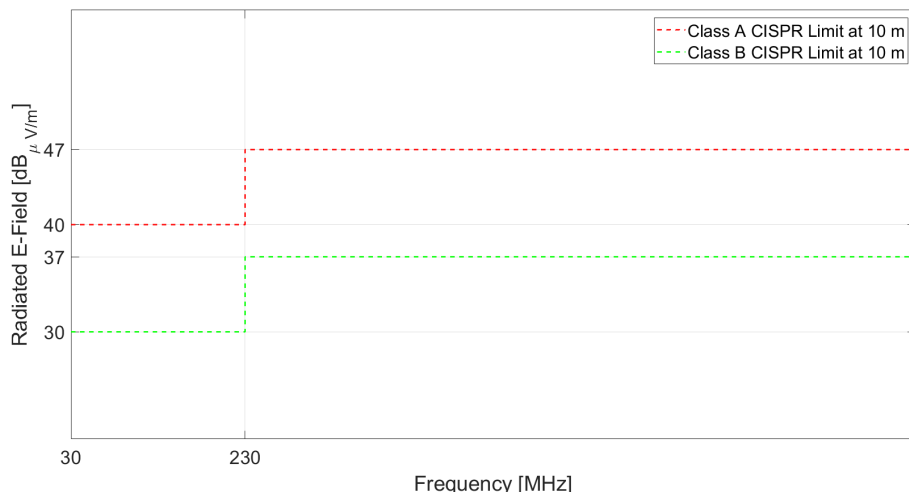


Figure 1.1: Radiated emission limits provided by CISPR at 10 m

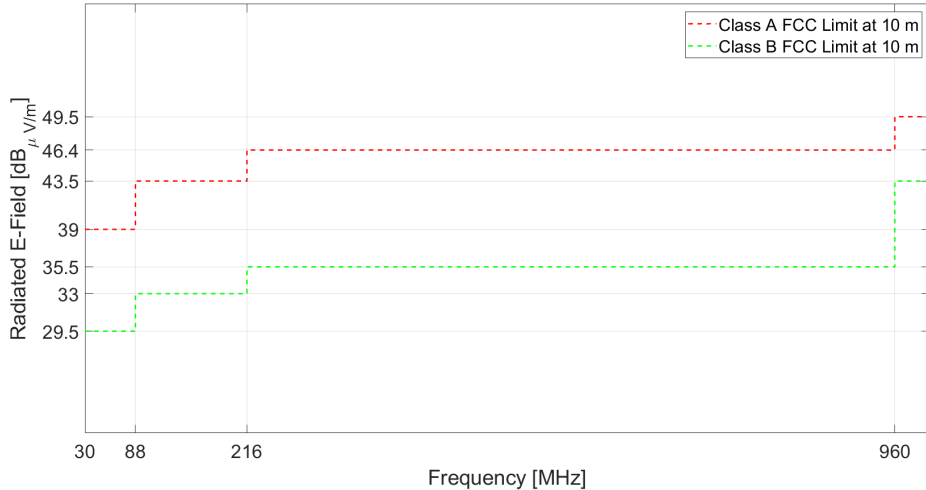


Figure 1.2: Radiated emission limits provided by FCC at 10 m

1.2.2 Electromagnetic Shielding

An electromagnetic shield is a metal enclosure that encloses an electronic device to prevent the emission of electromagnetic (EM) fields that could cause interference or non-compliance with regulatory limits. Shield effectiveness (SE) is defined as the ratio between the incident field and the field transmitted through the shield, expressed in decibels (dB):

$$SE = 20 \log \left(\frac{E_i}{E_t} \right) \quad (\text{for the electric field}) \quad (1.11)$$

$$SE = 20 \log \left(\frac{H_i}{H_t} \right) \quad (\text{for the magnetic field}) \quad (1.12)$$

Where E_i and H_i are the incident electric and magnetic fields and E_t and H_t are the transmitted fields. The effectiveness of the shielding is influenced by three main mechanisms: reflection loss (R), absorption loss (A) and multiple reflection loss (M):

$$SE = A_{dB} + R_{dB} + M_{dB} \quad (1.13)$$

Absorption Loss (A)

The absorption loss is related to the skin effect, which causes exponential attenuation of the EM field as it propagates through a conductive material. According to the skin effect, the incident EM field is exponentially attenuated as:

$$E \propto e^{-\frac{z}{\delta}} \quad (1.14)$$

Where $\delta = 1/\alpha$ is the skin depth, defined as:

$$\delta = \frac{1}{\alpha} = \frac{1}{\sqrt{\pi f \sigma \mu}} \quad (1.15)$$

Where:

- α is the attenuation constant of the material;

- f is the frequency;
- σ is conductivity;
- μ is the magnetic permeability;

The skin depth is the distance at which the electrical field is attenuated of $\frac{1}{e}$. The absorption loss A in dB is:

$$A_{dB} = 20 \log \left(\frac{E_0}{E_0 e^{-\frac{t}{\delta}}} \right) = 8.69 \frac{t}{\delta} \quad (1.16)$$

Where t is the thickness of the shield. For example, a shield with thickness $t = 10\delta$ attenuates approximately 90 dB .

Reflection Loss (R)

The reflection loss is due to the impedance discontinuity between the free space and the shield material. The intrinsic impedance of the conductive material is:

$$|\eta| = \frac{|E|}{|H|} = \sqrt{\frac{\omega\mu}{\sigma}} \quad (1.17)$$

The reflection coefficient Γ and the transmission coefficient T are:

$$\Gamma = \frac{\eta - \eta_0}{\eta + \eta_0} \quad (1.18)$$

$$T = \frac{2\eta}{\eta + \eta_0} \quad (1.19)$$

where $\eta_0 = 377\Omega$ is the free space impedance. The reflection loss in dB is:

$$R_{dB} = 20 \log \left(\frac{\eta_0}{4\eta} \right) \quad (1.20)$$

Multiple Reflection Loss (M)

When the thickness t of the shield is not much greater than the depth of the skin, multiple reflections within the shield become significant. The total transmitted field is the sum of the multiple transmissions, i.e. the sum of the primary and secondary waves transmitted from the output interface of the conducting material:

$$E_t = E_{t1} + E_{t2} + E_{t3} + \dots \quad (1.21)$$

The effect of multiple reflections is described by:

$$M_{dB} = 20 \log \left| 1 - \left(\frac{\eta_0 - \eta}{\eta + \eta_0} \right)^2 e^{-2\gamma t} \right| \quad (1.22)$$

Where $\gamma = \alpha + j\beta$ is the complex propagation constant.

Shielding for Low Frequency Magnetic Fields

For far-field sources (uniform plane waves), shielding at low frequencies is dominated by reflection loss, while at high frequencies absorption loss prevails. For near-field electrical sources, the situation is similar: reflection is predominant at low frequencies, while absorption is predominant at high frequencies. For near-field magnetic sources, however, the situation is different. Absorption loss tends to be the main shielding mechanism at all frequencies, but both reflection and absorption are ineffective at low frequencies, necessitating alternative solutions such as:

- Magnetic flux deflection with high permeability materials: this is achieved by using a screen made of ferromagnetic material with high permeability, which channels the magnetic field within its structure and deflects it away from the protected region;
- Shorted-turn method: a conductive circuit is positioned so that the incident magnetic field induces a current in the loop, generating an opposite magnetic flux that attenuates the overall field in the surrounding area.

Aperture Effect

Openings in the shields, such as those for ventilation, can reduce the effectiveness of the shielding. To minimise this effect, many small openings or waveguides are used below the cut-off frequency. The shielding effectiveness afforded by one guide is:

$$SE_{dB} = 27.3 \frac{l}{d} \quad (1.23)$$

where l is the length of the rail and d is the cross-sectional dimension.

1.3 Simulation Software and Setup

The software used was CST Studio Suite, an advanced software for electromagnetic simulation, which is particularly suited to analyzing electromagnetic propagation and radiation phenomena, allowing the evolution of electromagnetic fields to be observed in the time or frequency domain.

One of the main advantages exploited by CST is the possibility of performing parametric sweeps, which allow the dimensions and properties of components, such as antennas, to be optimized to achieve the desired performance. In addition, the software offers tools for evaluating reflection coefficient, radiation patterns and radiated emissions, making it ideal for studies related to electromagnetic compatibility (EMC).

CST, by also integrating functionality for the design of shielding structures, allows to analyse the effect of openings or discontinuities on emission levels.

1.3.1 Model Configuration and Dipole Length Optimization

The initial objective is to optimise the length L of a dipole, consisting of two cylinders as shown in Fig. 1.3, by means of simulations.

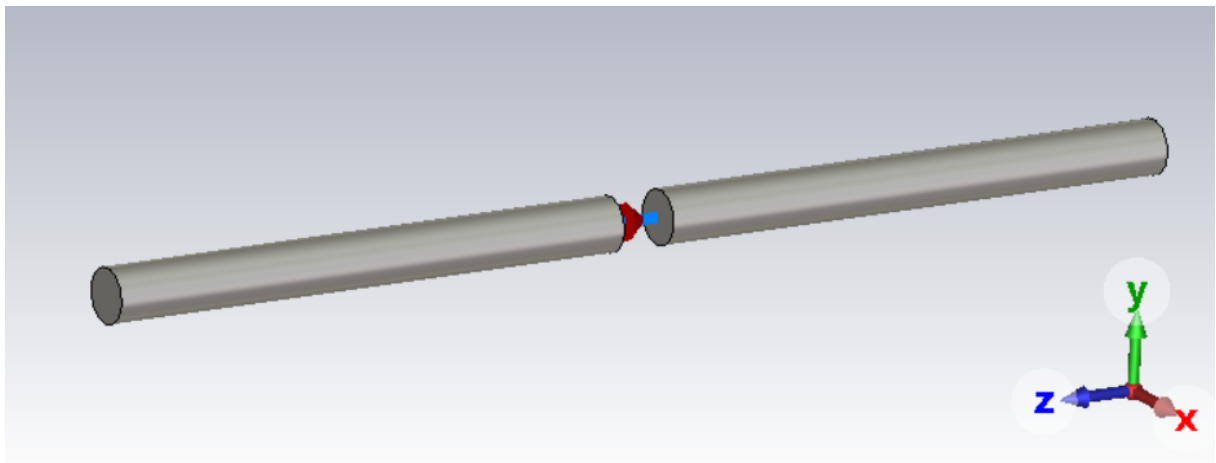


Figure 1.3: 3D model of a single dipole

The dipole is designed to operate at the frequency of 5 GHz , and the optimisation is aimed at reducing the reflection coefficient S_{11} at the frequency of interest, ensuring better impedance matching. The parameter S_{11} , known as the input reflection coefficient, is one of the scattering parameters (S-parameters) used to describe the degree of matching of an antenna as a function of power. Defined as the ratio of the reflected power to the incident power on a port, S_{11} measures how much of the power sent to a port is reflected back. Optimisation was carried out by progressively varying the length of the dipole, keeping the cylinder radius and the gap between the two constant. The frequency range over which the analysis was carried out is between 3 GHz and 7 GHz , in order to center the frequency of interest.

The initial parameters used for the simulation are shown in Table 1.1. These include the operating frequency, the speed of light, the excitation current of the discrete port of the dipole, the wavelength, the radius of the cylinders and the gap between the two elements of the dipole.

In order to optimize L , we carried out simulations in which the length of the dipole was progressively increased to achieve the lowest possible value of the S_{11} parameter at 5 GHz .

Table 1.1: List of the constant design parameters

Name	Expression	Value	Description
f	-	$5 \cdot 10^9 \text{ Hz}$	Frequency
c	-	$3 \cdot 10^8 \text{ m/s}$	Speed of Light
I	-	1 mA	Current
λ	c/f	59.95 mm	Wavelength
r	$0.01 \cdot \lambda$	0.5995 mm	Radius
g	$0.02 \cdot \lambda$	1.199 mm	Gap

The simulations began by identifying a range within which to vary the length L . The starting point was $\lambda/2 = 29.975 \text{ mm}$, a typical choice to ensure good impedance matching in dipole antennas, while the upper limit was set at $\lambda/2.5 = 23.998 \text{ mm}$.

As shown in Fig. 1.4, the optimal dipole length was obtained at $\lambda/2.36 = 25.402 \text{ mm}$, with a minimum S_{11} at the target frequency of 5 GHz.

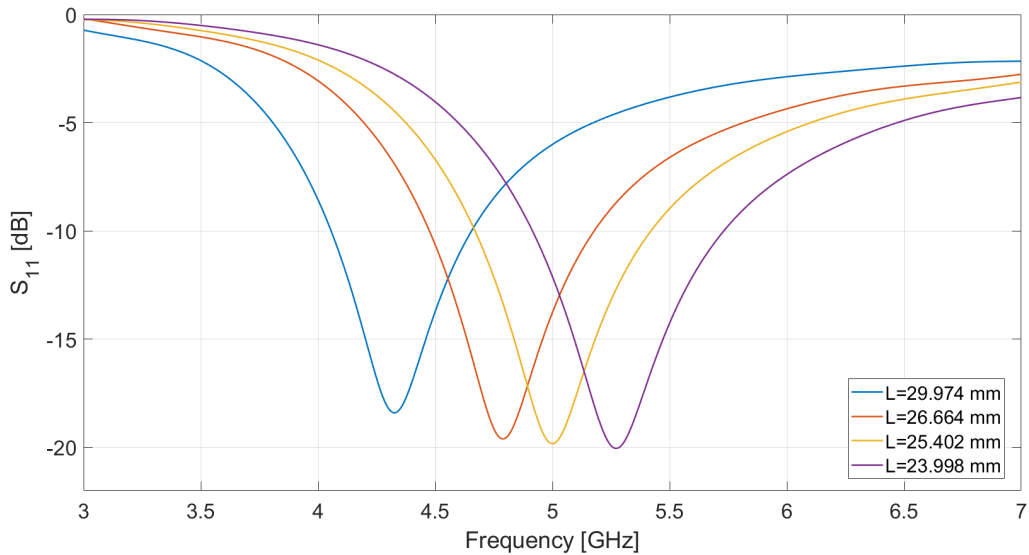


Figure 1.4: S_{11} parameter as a function of frequency for a dipole antenna with varying lengths (23.998 \div 29.974 mm)

1.4 Two Dipoles Model

1.4.1 Model Configuration

The analysis was extended by adding a second dipole, compared to the previous system, at a distance of $s = \lambda/8 = 7.493\text{ mm}$ from the first one. The goal was to examine the effect of exciting both dipoles in common mode and differential mode on the overall performance of the antenna. In particular, the impact of the excitation configuration on the radiated field distribution was studied by analyzing the 3D polar patterns in both excitation modes and comparing their values with the limits imposed by CISPR at 10 m. The two dipoles have the same physical characteristics described in the previous analysis and are placed in a parallel configuration along the z-axis. Each dipole was excited simultaneously in both modes. The system was analyzed under two different excitation modes:

- **Common Mode (CM):** In this mode, both dipoles are excited with the same in-phase current. This means that the current on both dipoles has the same magnitude and direction, as represented by the model in Fig. 1.5;

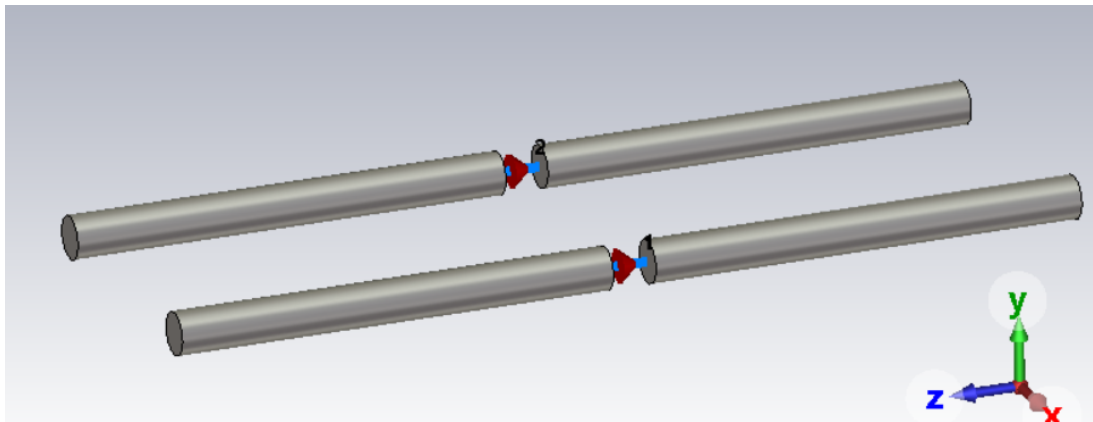


Figure 1.5: 3D model of double dipoles with current excitation in common mode

- **Differential Mode (DM):** In this mode, the dipoles are excited with currents of equal amplitude but opposite polarity (Fig. 1.6).

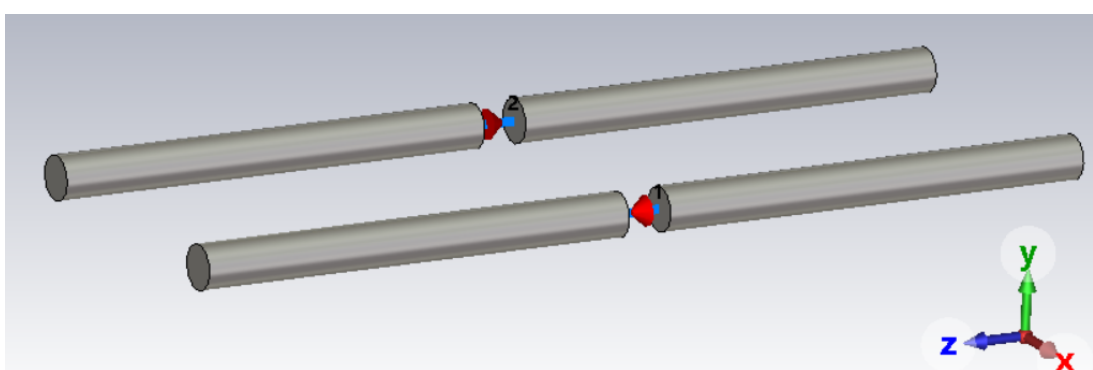


Figure 1.6: 3D model of double dipoles with current excitation in differential mode

1.4.2 Simulation

After completing the configuration phase, simulations were carried out to determine the radiated field values in the two operating modes. The analysis was conducted over a frequency range from 3 GHz to 7 GHz , with an increment of 500 MHz at each step. During the simulations, both dipoles were fed with a current of 1 mA in magnitude.

Common Mode Current

The simulation made it possible to characterize the far-field generated by the system operating at a frequency of 5 GHz . The results obtained show a behavior consistent with the theoretical model described by Equation (1.7), which defines the spatial distribution of the radiated electric field \bar{E}_{tot} , as shown in Fig. 1.7.

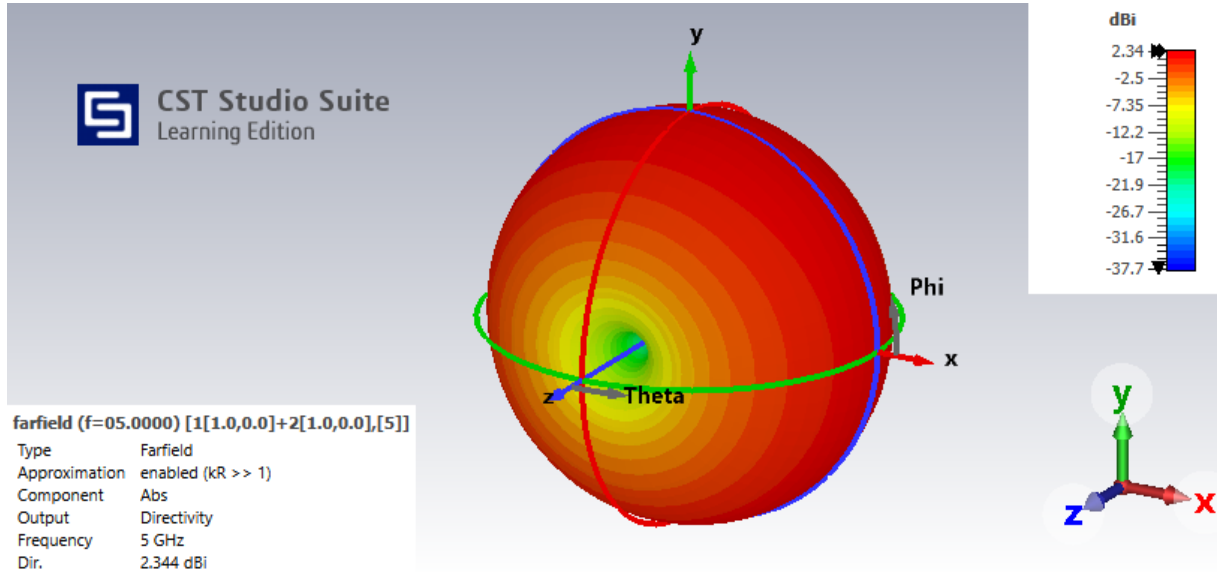


Figure 1.7: 3D radiation pattern at 5 GHz of two dipoles in common mode

The far-field plot highlights that the maximum directivity, equal to 2.344 dB_i , occurs at $\theta = 90^\circ$ in the xy -plane (Azimuth). This result is consistent with the fact that the distance between the two dipoles is significantly smaller than the wavelength ($s \ll \lambda$). In our specific case, where $s = 7.493\text{ mm}$ compared to a wavelength of 59.95 mm , the term $\cos(\beta \frac{s}{2} \cos \phi) \rightarrow 1$, resulting in maximum radiation in the Azimuth plane (perpendicular to the dipole axis), i.e., for $\theta = \frac{\pi}{2}$, regardless of the chosen angle ϕ .

The behavior of the field as a function of distance follows the expected trend, with a decay proportional to $\frac{1}{r}$, as described by the term $\frac{e^{-j\beta r}}{r}$ in the equation.

Differential Mode Current

Let us now evaluate what happens in differential mode by analyzing the radiation pattern of the dipole pair at 5 GHz , starting from Equation (1.10). Unlike the common mode configuration, the out-of-phase excitation (180° phase shift) produces a different radiation behavior.

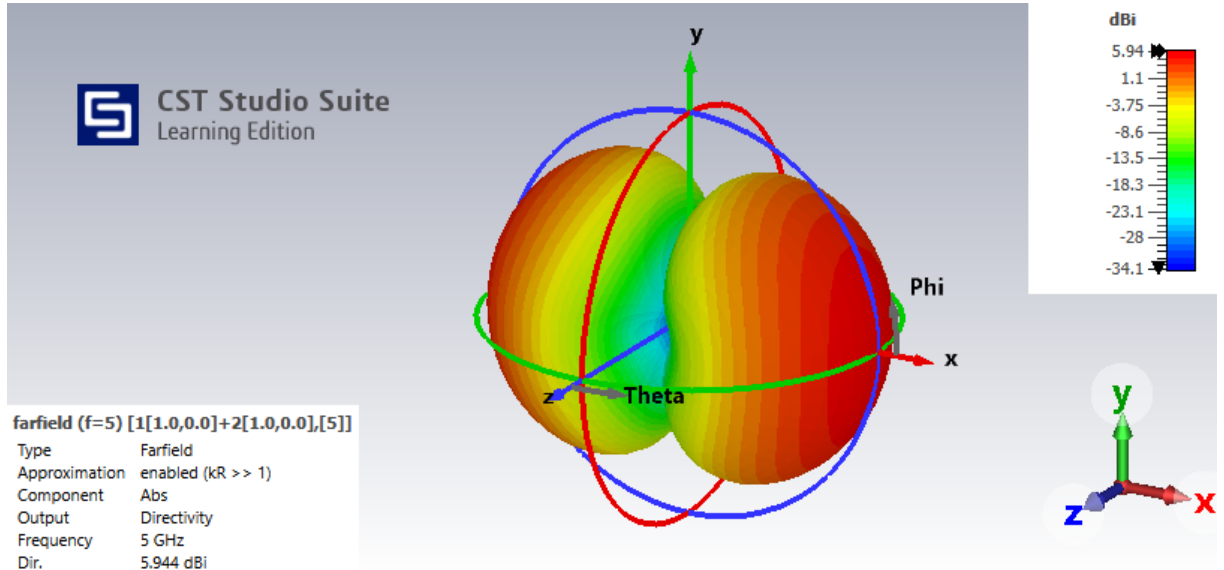


Figure 1.8: 3D radiation pattern at 5 GHz of two dipoles in differential mode

The 3D pattern of the radiated field, in Fig. 1.8, shows a maximum directivity of 5.944 dB_i along the x axis ($\theta = \frac{\pi}{2}$, $\phi = 0$). The distance between dipoles $s = 7.493$ mm $\ll \lambda$ justifies the radiation pattern, with a null field along the z axis ($\theta = 0^\circ, 180^\circ$) and the y axis ($\phi = 90^\circ, 270^\circ$). Power level analysis shows a decay of the field proportional to $\frac{1}{r}$, as in the previous case.

1.4.3 Results

Common Mode Current

The graph in Fig. 1.9 shows how the electric field radiated by the system behaves with respect to the CISPR regulatory limits at 10 meters. On the horizontal axis we see the frequencies under consideration, ranging from 3 GHz up to 7 GHz, while the vertical axis shows the radiated electric field strength, expressed in $dB_{\mu V/m}$. The blue line shows the actual electric field strength radiated by the system: it is evident that this line is consistently above both limits, starting at about 74 $dB_{\mu V/m}$ and gradually increasing to about 84 $dB_{\mu V/m}$ as frequency increases. This increasing trend indicates that the system tends to emit higher levels of electric field at higher frequencies, so system emissions are well beyond acceptable values in both industrial (Class A) and residential (Class B) environments. This behavior indicates the need to introduce countermeasures to bring the radiated field within limits, including shielding, analyzed next.

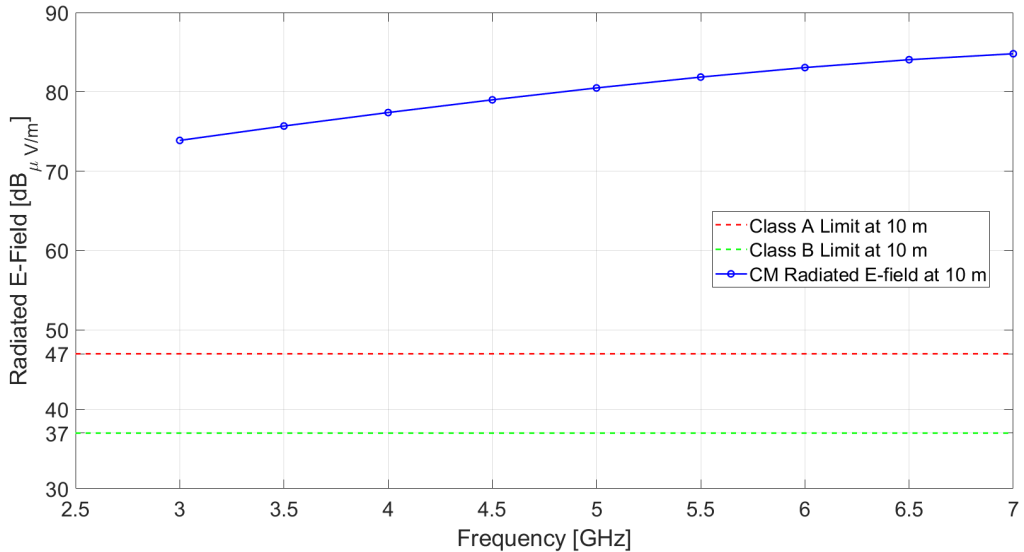


Figure 1.9: Radiated electric field for a couple of dipoles in common mode with respect to CISPR emission limits for Class A and B, in $3 \div 7 \text{ GHz}$ frequency range

Differential Mode Current

In this graph, Fig. 1.10, we see depicted the radiated electric field in differential mode measured at a distance of 10 m. Compared to the previous graph, the emission levels here are a bit lower, but still well above the regulatory limits. The radiated field starts at about $61 \text{ dB}_{\mu\text{V/m}}$ at 3 GHz and gradually increases to near $81 \text{ dB}_{\mu\text{V/m}}$ around 7 GHz . Again, the increasing trend with frequency is evident, suggesting that emissions worsen with increasing frequency. Again, countermeasures need to be taken.

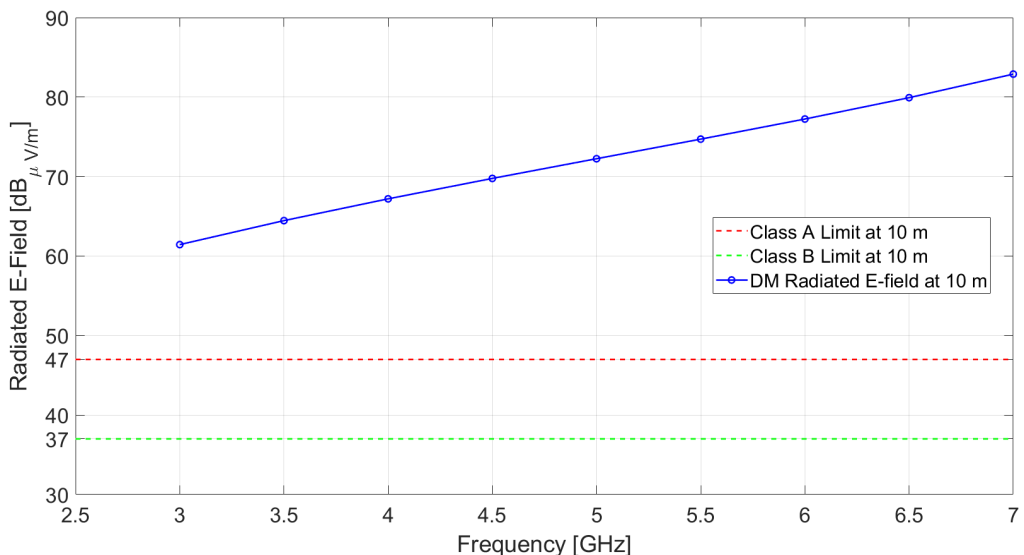


Figure 1.10: Radiated electric field for a couple of dipoles in differential mode with respect to CISPR emission limits for Class A and B, in $3 \div 7 \text{ GHz}$ frequency range

1.5 Shield Box Model

In the previous chapter, the electromagnetic behavior of a dipole pair was analyzed, highlighting how the overall radiative emissions exceed the limits imposed by electromagnetic compatibility standards. This scenario calls for strategies to mitigate unwanted interference and ensure compliance with standards, such as shielding.

1.5.1 Model Configurations

In the context of mitigating electromagnetic emissions generated by a dipole pair, the adoption of a Perfect Electric Conductor (PEC) shield proved to be an effective solution to ensure compliance with the limits imposed by CISPR. PEC, being an ideal material with infinite conductivity, acts as a perfect barrier to electromagnetic fields, completely reflecting incident waves and preventing their propagation into the surrounding environment.

As shown in Fig. 1.11, the two dipoles are positioned symmetrically and centrally within the shield box.

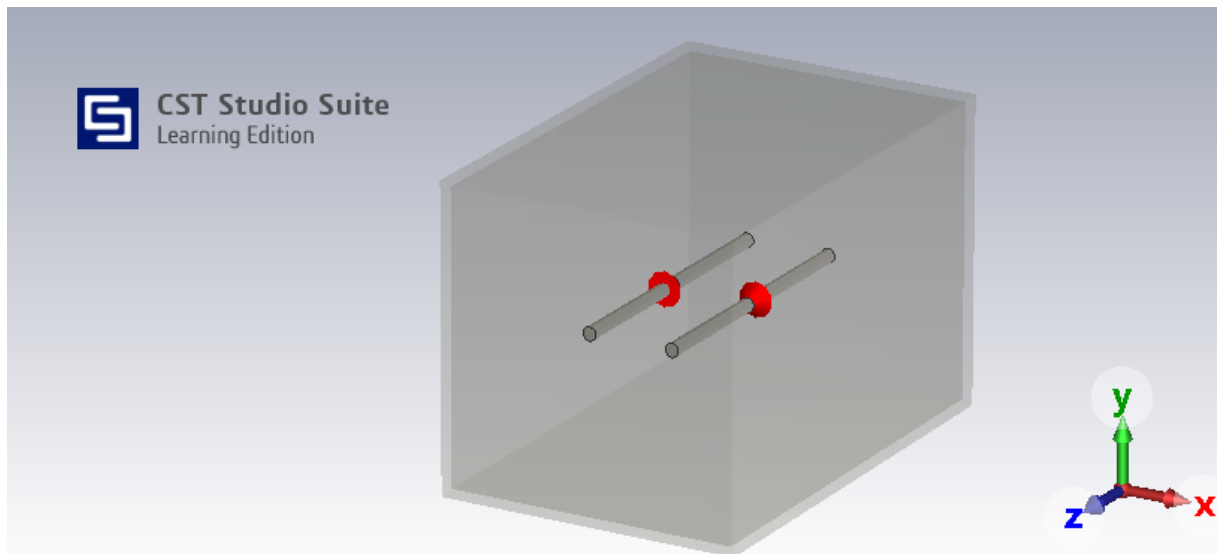


Figure 1.11: 3D model of a PEC shield box containing a couple of dipoles in differential mode

The exact dimensions of the box are given in Tab. 1.2, which provides the data needed to reproduce the configuration used in simulations and experimental measurements.

Table 1.2: List of the shielding box building parameters

Name	Expression	Value	Description
w_box	L	25.402 mm	Width
L_box	L	25.402 mm	Length
h_box	$1.5 \cdot L$	38.103 mm	Height
t_box	$0.01 \cdot \lambda$	0.5995 mm	Thickness

1.5.2 Simulation and Results

Experimental analyses showed that the implementation of the shield in PEC results in total suppression of unwanted electromagnetic emissions. The collected data, showed in Fig. 1.12, illustrate the trend of the radiated electric field as a function of frequency, in the $3 \div 7 \text{ GHz}$ range, comparing the shielded configuration and the CISPR regulatory limits for Classes A and B at 10 m distance.

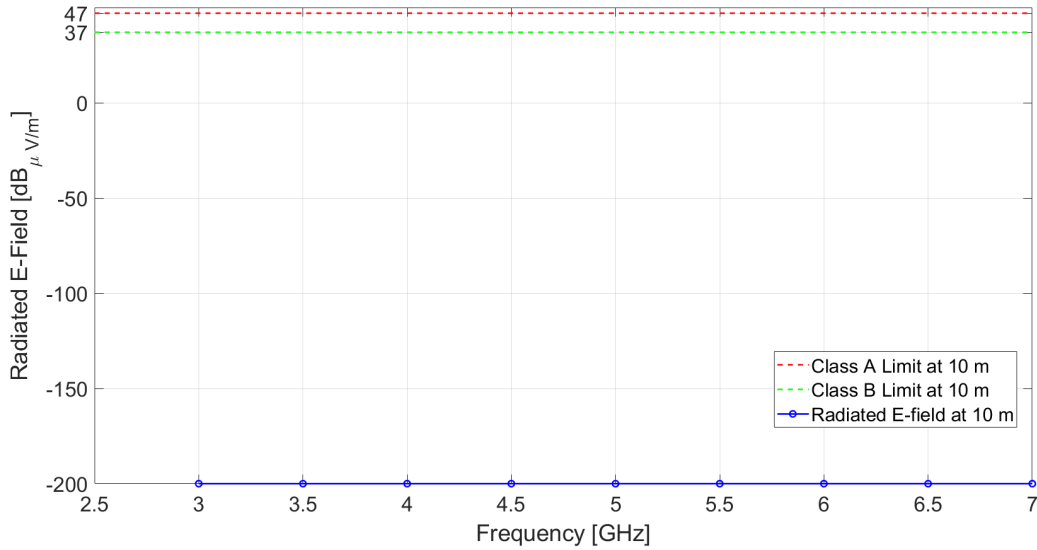


Figure 1.12: Radiated electric field for a couple of dipoles in differential mode in a PEC shielding box with respect to CISPR emission limits for Class A and B, in $3 \div 7 \text{ GHz}$ frequency range

This result can be attributable to the electrodynamic properties of the material: the ideally infinite electrical conductivity of PEC cancels out the skin depth, preventing the penetration of the field inside the metal and generating a total reflection of the incident waves.

1.6 Shield Box with Aperture Model

While ideal metal shielding provides high suppression of electromagnetic emissions, the presence of openings, which are necessary for functional purposes such as ventilation, can significantly impair its effectiveness. This section will examine the effects of a discontinuity in the shielding of a dipole pair, focusing on the characteristics of the field radiated through a square aperture.

1.6.1 Model Configurations

As shown in Fig. 1.13, a square aperture was placed on the shield box, analysed above, perpendicular to the side of maximum radiation of the dipole pair, i.e. the x axis.

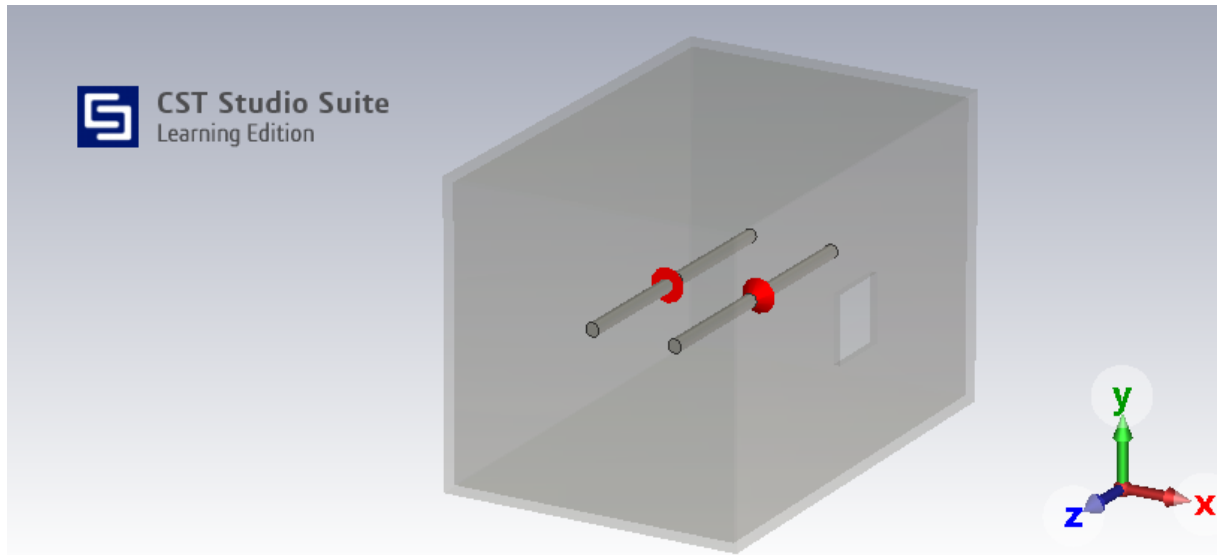


Figure 1.13: 3D model of a PEC shield box with square aperture containing a couple of dipoles in differential mode

Analysis of the effects of an aperture in metal shielding has focused on the relationship between its size and the emitted electric field. Specifically, the design of the aperture is based on a proportional relationship that links the length of the side of the aperture itself to a constant called α . The latter represents a factor of division, the value of which determines the reduction of the size of the aperture with respect to the wavelength λ of the electromagnetic signal radiated by the dipoles. As illustrated in Tab. 1.3, the values assumed by the constant α were chosen to cover a wide range of dimensions. The length of the side of the opening, denoted by l , is defined by the relation $l = \lambda/\alpha$. Consequently, as α increases, the size of the opening decreases, allowing the influence of different size openings on the shielding performance of the structure to be evaluated.

For instance, the larger aperture side is obtained by dividing the wavelength λ by an $\alpha = 3$, while the smaller by dividing λ by $\alpha = 32$. The other values can be calculated in the same fashion.

Table 1.3: List of the aperture building parameters

Name	Expression	Value	Description
α	-	[3, 4, 6, 8, 10, 12, 16, 24, 32]	Division factor
l	λ/α	[19.98, 14.99, 9.99, 7.49, 5.99, 4.99, 3.75, 2.5, 1.87] mm	Aperture side

1.6.2 Simulation

The simulations conducted allowed us to study the behavior of the radiated field generated by a pair of dipoles operating in differential mode, enclosed in a shielding structure equipped with an aperture. The results obtained show that the discontinuity introduced by the aperture significantly affects the field distribution, with detectable effects on directivity, signal attenuation and overall radiation pattern. An example is represented in Fig. 1.14 and 1.15 where the side of the aperture l is equal to 5.99 mm .

At the operating frequency of 5 GHz , the system exhibits a maximum directivity in the expected direction ($\theta = 90^\circ, \phi = 0^\circ$) and reveals a progressive gain decay in the opposite direction ($\theta = 270^\circ, \phi = 180^\circ$).

From a physical point of view, the aperture acts as a secondary source of radiation, allowing the field generated by the dipoles to couple with the external environment.

The attenuation observed in the lateral directions confirms that the metal shielding succeeds in containing emissions, even in the presence of the aperture.

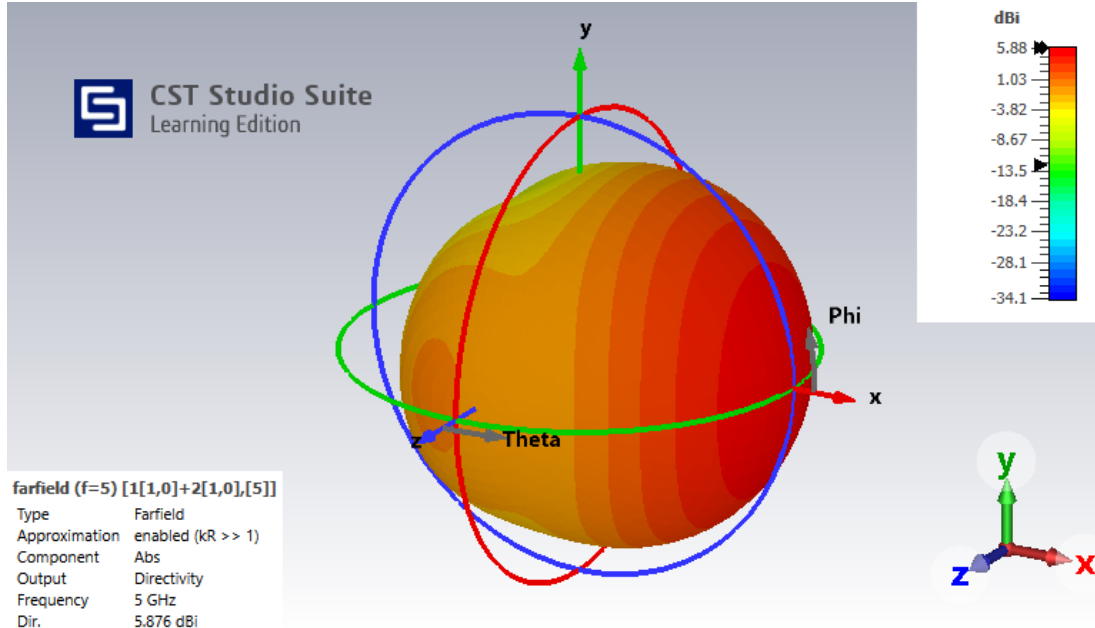


Figure 1.14: 3D radiation pattern at 5 GHz of two dipoles in differential mode contained in a shielding box with $\lambda/10$ side square aperture from main lobe view

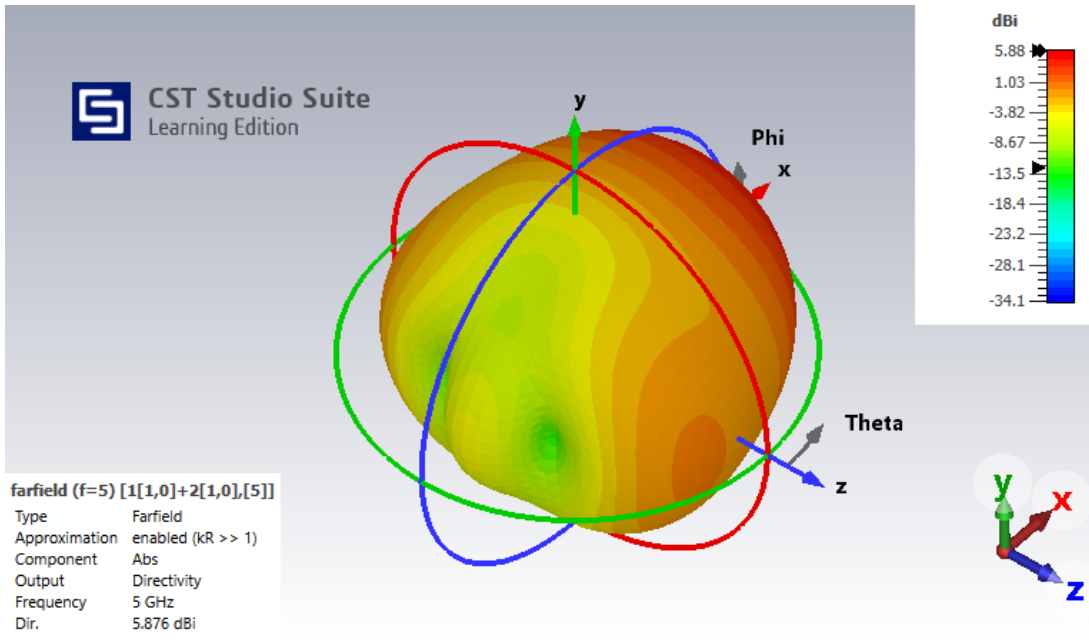


Figure 1.15: 3D radiation pattern at 5 GHz of two dipoles in differential mode contained in a shielding box with $\lambda/10$ side square aperture from back lobe view

1.6.3 Results

Fig. 1.16 shows the trend of the radiated electric field over a frequency range of 3 to 7 GHz generated by a pair of dipoles operating in differential mode, positioned inside a metal shield equipped with a square aperture of varying size. The data presented include several measurements of the side of the aperture, ranging from 1.87 mm up to 19.98 mm, and compare the radiated field levels with the Class A and B reference limits imposed by CISPR.

The presence of an aperture in the shielding can compromise electromagnetic isolation, allowing the field to leak out. The size of the opening plays a crucial role: wider openings reduce shield effectiveness leading to greater field leakage and exceeding imposed limits, while narrower openings mitigate it by making the system compliant with regulations.

Analyzing the data in Fig. 1.16, it is observed that the first aperture, which allows emissions to be confined below Class A limits at 10 meters, has a side length of 4.99 mm ($\lambda/12$). However, the size of the aperture is still found to be too large for residential environments: this is shown by the purple curve that exceeds the limits imposed for Class B devices starting from about 6 GHz.

The first curve, on the other hand, found to be compliant with both limits imposed by CISPR is the yellow one, and corresponds to a side opening of 3.75 mm ($\lambda/16$).

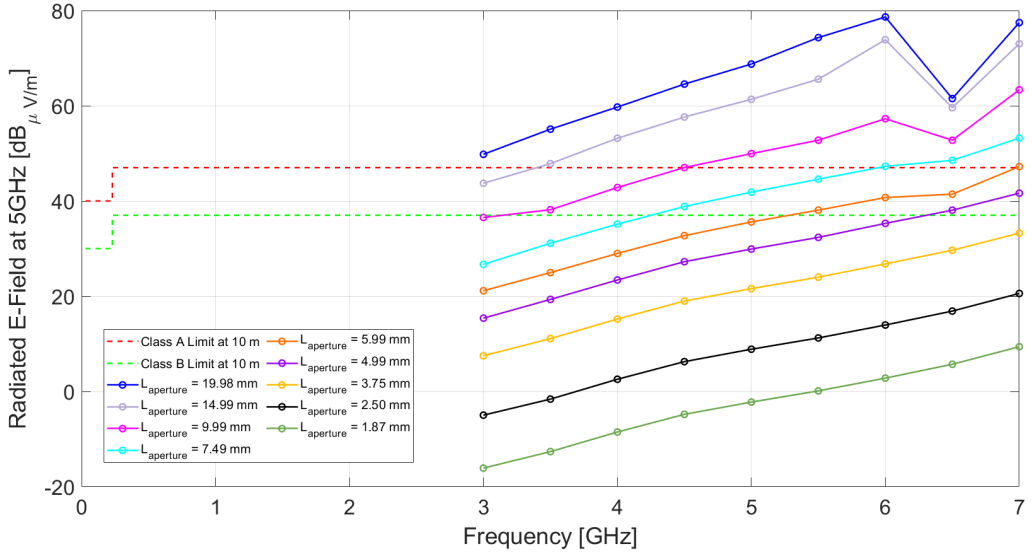


Figure 1.16: Radiated electric field for a couple of dipoles in differential mode in a PEC shielding box with variable side aperture length with respect to CISPR emission limits for Class A and B, in $3 \div 7$ GHz frequency range

In Fig. 1.17 the electric field radiation is analyzed, considering the single frequency of 5 GHz, in relation to the size of the square aperture side, varying between 1.87 mm and 14.99 mm. The amplitude of the field shows nonlinear growth as the size of the aperture increases, with behavior attributable to the increased outflow of electromagnetic energy. The simulation shows that compliance with the more restrictive Class B at 37 $dB_{\mu V/m}$, requires an aperture sizes less equal than 6.28 mm, a value corresponding to the point of intersection between the radiated field curve and the green dashed line. For Class A, the limit at 47 $dB_{\mu V/m}$ is exceeded when an aperture side greater than 9.01 mm, as indicated by the intersection with the red line. Below 6 mm, the emission remains within the margins of both classes, providing an effective shielding in any case.

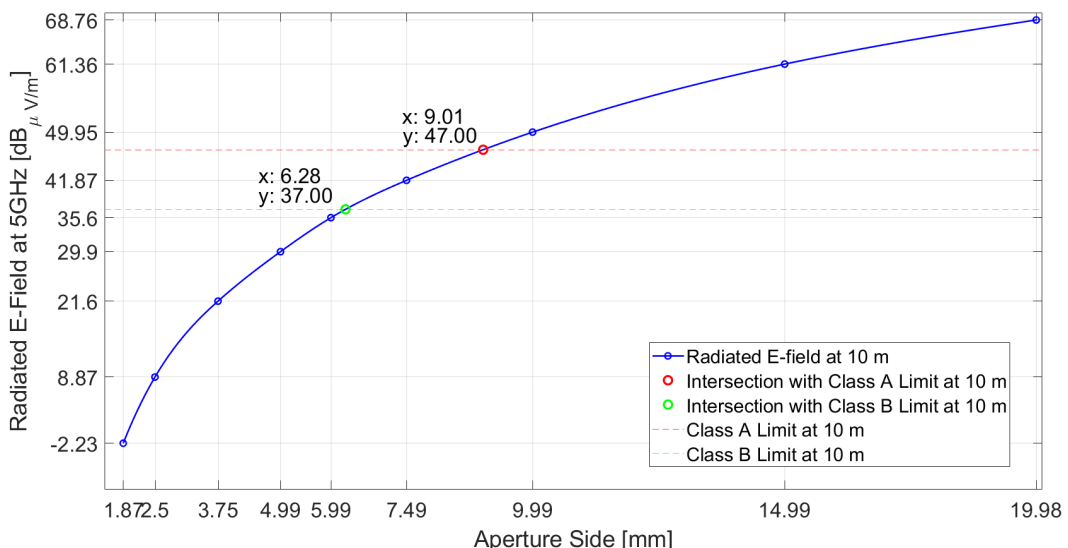


Figure 1.17: Radiated electric field for a couple of dipoles in differential mode in a PEC shielding box with variable side aperture length with respect to CISPR emission limits for Class A and B at 5 GHz

1.7 Conclusion

The study on radiated emissions of electric dipoles in shielded systems focused on the mechanisms of electric field propagation, with a focus on the interaction between shield geometry and electromagnetic compatibility (EMC) performance.

Three scenarios were compared in the analysis: no shielding, full shielding, and partial shielding with openings. In the absence of shielding, dipoles showed the highest emission levels, aligned with theoretical models, while full shielding zeroed out emissions.

The most relevant configuration, those with openings, revealed hybrid behaviors, in which aperture sizes alter emissions. It was found that targeted design choices, such as reduced apertures, can significantly reduce unwanted emissions, facilitating compliance with CISPR regulatory limits for Classes A and B.

This stresses the need to balance structural integrity of shielding and functional requirements, such as ventilation or cable routing, to optimize EMC performance.

Chapter 2

Design and Analysis of Microstrip Patch Antenna Arrays

Microstrip patch antennas represent one of the most popular solutions in modern wireless communication systems due to their compact design, low profile, and ease of integration with printed circuit boards. These radiating elements, typically fabricated on dielectric substrates, offer excellent design flexibility, allowing their radiative characteristics to be controlled through careful choice of parameters such as geometric shape, substrate material and feed method.

This work initially focuses on analyzing, through the Antenna Toolbox offered by MATLAB, the fundamental properties of the single-patch antenna, examining in particular the relationship between geometry, substrate parameters and behavior at the 5 GHz frequency. Building on this foundation, the study extends to the design, through MATLAB's Phased Array System Toolbox, of array configurations, where multiple patches are arranged in precise patterns to improve directivity, gain and beamforming capabilities.

2.1 Simulation Goals

The main goals of this chapter are:

- **Microstrip Patch Parameter Optimization:** using the Antenna Designer, optimization of the basic parameters of a microstrip patch antenna, such as patch length and width, ground plane dimensions and feed offset, in order to achieve matched impedance and good radiating efficiency at the working frequency (5 GHz).
- **Design and analysis of a Uniform Linear Array (ULA) with zero phase shift:** design a ULA with equidistant elements and in-phase feeding (zero phase shift), varying the number of antennas to study their impact on the radiation pattern by analyzing the main lobe and side lobe parameters.
- **Design and analysis of a ULA with variable phase shift:** design a uniform linear array with a fixed number of antennas but with variable phase shift between elements, allowing the effect of phase shift on the direction of the main lobe (beam steering) to be observed.
- **Design and analysis of a broadside binomial tapered array:** design an array with binomial distribution of feed amplitudes, maintaining the broadside radiation

direction and evaluation the side lobe reduction and array gain, varying the number of antennas;

- **Design and analysis of a broadside Chebyshev tapered array:** design of a Chebyshev array by setting a side lobe level (SLL) and varying the number of antennas, followed by an evaluation about the possibility to control the side lobe suppression;
- **Performance comparison of the three types of arrays:** comparison between the results obtained from the three arrays configuration in terms of: main lobe magnitude, direction and width, side lobe magnitude and SLL.

2.2 Background

2.2.1 Patch Microstrip

Microstrip patch antennas are compact, lightweight devices consisting of a metal surface (the patch) printed on a thin dielectric substrate, below which is a ground plane.

This type of antenna is widely adopted because of its many advantages: in addition to low cost and low weight, they offer small footprints, are easily fabricated using standard photolithography techniques, and can also be installed on curved or irregular surfaces, thus adapting to portable or wearable devices. Another important feature is design versatility: patches of different shapes (rectangular, circular, triangular, etc.) can be fabricated, each with specific electromagnetic properties and with the ability to support different polarizations [1]. They can also be designed to operate on multiple frequencies, making them suitable for dual-band or multi-band systems [2].

However, the basic configuration of microstrip antennas also has limitations: relatively narrow bandwidth, which reduces flexibility in dynamic or wideband environments, low efficiency and gain, polarization purity, and limited power handling capabilities.

One of the most common problems is spurious radiation, or unwanted signals radiated outside the band of interest, which can interfere with other nearby systems. These emissions can result from unwanted couplings or complex power system geometries. Similarly, spurious losses, i.e., energy losses in unintended paths within the substrate or to non-radiating elements of the antenna, can occur, reducing the overall efficiency of the system [3].

A key element in the design of these antennas is the feeding technique, which determines how the signal is transferred to the patch. Among the most common techniques is the coaxial probe, which establishes a direct connection between the patch and a coaxial line, a simple solution but suitable mainly for thin substrates. Another option is the use of a microstrip line, where a conductive strip feeds the patch directly; this configuration is easy to integrate but tends to be more prone to surface waves and spurious radiation, especially with thick substrates. An alternative approach is aperture coupling, which uses a gap in the ground plane to transfer the signal, improving the separation between the power supply and the radiating element and reducing unwanted radiation. Finally, proximity coupling enables electromagnetic energy transfer without direct contact, offering advantages such as higher bandwidth and lower spurious losses compared with other [1] techniques.

Because of these features, microstrip antennas are widely used in numerous applications: from mobile and satellite communications to GPS, RFID, WiMax and radar [2].

2.2.2 Antenna Array

An antenna array is a structure composed of several radiating elements arranged in a pre-determined geometric configuration and fed in a suitably controlled manner. The main advantage of this type of configuration is the possibility of flexibly modelling the radiation pattern, exploiting techniques such as beamforming and beamsteering. In particular, by varying the number of elements in the array, it is possible to adjust the width of the main lobe: a greater number of antennas allows it to be narrower, increasing directivity and angular resolution; conversely, a smaller number results in a wider lobe and less focused energy. By acting on the phases of the feed signals, on the other hand, it is possible to electronically orient the radiated beam in the desired direction, without any need for mechanical movement.

Considering all the radiating elements of the array equal to each other, the antenna factor is equal for all N elements. The total field formula can be written as:

$$\overline{E}(P) = jk_0\eta_0 \cdot \frac{e^{-jk_0r}}{4\pi r} \cdot \underbrace{\vec{F}(\theta, \phi)}_{\text{Antenna Factor}} \cdot \underbrace{\sum_{n=1}^N |I_n| \cdot e^{-j\theta_n} \cdot e^{jk_0(r_n \cdot a_r)}}_{\text{Array Factor}} \quad (2.1)$$

where:

- I_n : excitation current modulus of the n^{th} element;
- $e^{-j\theta_n}$: current phase of the n^{th} element;
- $k_0 = \frac{2\pi}{\lambda}$: wave number in vacuum;
- η_0 : characteristic impedance in vacuum
- r : distance between the array and the observation point P ;
- e^{-jk_0r} : propagation factor of the n^{th} element;
- $\vec{F}(\theta, \phi)$: antenna factor of the single radiating element;
- $e^{jk_0(r_n \cdot a_r)}$: progressive phase shift due to the relative position of the n^{th} element;
- $4\pi r$: free space path loss factor;

Then the formula of the total field can be written as the product between the Antenna Factor and the Array Factor.

ULA Array

The Uniform Linear Array (ULA) is the simplest antenna array configuration that can be obtained with an array of N elements. The array is called uniform because it is characterized by:

- N antenna elements aligned along a certain direction (e.g., x -axis);
- Equally spaced antenna elements with distance d ;
- Equal feeding current intensity for each antenna element;
- Constant phase shift between adjacent antennas.

The expression of the array factor can be rewritten as:

$$F(\theta, \phi) = I_0 \sum_{n=0}^N e^{-j\varphi_n} \cdot e^{jk_0nd\cos\psi} = I_0 \sum_{n=0}^N e^{jn(u-u_0)} \quad (2.2)$$

where:

- I_0 : current modulus, equal for each antenna element;
- n : n^{th} antenna element of array;
- $e^{-j\varphi_n}$: phase of the current of the n^{th} antenna element;
- $e^{jk_0nd\cos\psi}$: spatial propagation term;
- ψ : angle formed between the axis of the antenna array and the direction vector from the array to the observation point P ;
- $u = k_0d\cos\psi$: phase difference between adjacent antenna elements resulting from the spatial propagation of the electromagnetic wave;
- $u_0 = \frac{\varphi_n}{n}$: incremental current phase difference between neighboring elements;

By expanding the summation as a geometric series, we can obtain the expression of array factor:

$$|F(u)| = I_0 \left| \frac{\sin((\frac{N+1}{2}) \cdot (u - u_0))}{\sin \frac{(u - u_0)}{2}} \right| \quad (2.3)$$

Normalizing the function with respect to the amplitude of the current, we get:

$$\frac{|F(u)|}{I_0} = \left| \frac{\sin((\frac{N+1}{2}) \cdot (u - u_0))}{\sin \frac{(u - u_0)}{2}} \right| \simeq \frac{\sin((N+1)x)}{\sin x} \quad (2.4)$$

When $u \rightarrow u_o$, both numerator and denominator tend to zero. In this limit, approximating the function \sin by its argument, we obtain that the array factor reaches its maximum value, proportional to $(N+1)I_0$. This occurs at $u = u_0$, which defines the direction of the main lobe, centered in u_0 .

The function has a period of 2π , which means that the replicas of the main lobe are centered in $u_0 + 2k\pi$ with $k = 1, \dots, N$.

The distance d between array elements plays a crucial role in determining the visible space and the accuracy of the radiation pattern. For a ULA, the visible space is defined in the range:

$$-k_0d \leq u \leq k_0d \quad (2.5)$$

where $u = k_o d \cos \psi$. This occurs due to the range of values of the cos function, which varies between -1 and 1, so $\cos \psi$ can only take values in this range, and thus the visible range varies from 0° to 180° . If the spacing d is excessive ($d > \lambda/2$), spatial aliasing occurs, causing the main and side lobes to overlap in the radiation pattern, resulting in a reduction in the overall efficiency of the array. To avoid aliasing, the element spacing d must satisfy the condition: $d \leq \lambda/2$. This limit ensures that the visible space is maximised and that the radiation pattern accurately represents the spatial distribution of the signal. Increasing d beyond this limit does not improve performance and introduces undesirable effects such as spatial aliasing.

The secondary lobes, however, are centered in:

$$u_{rel.\max.} = u_0 + \underbrace{\frac{2m\pi}{N+1}}_{\text{zero position}} + \underbrace{\frac{1}{2} \frac{2\pi}{N+1}}_{\text{half distance between zeros}} \quad (2.6)$$

The ratio between the main lobes and the secondary lobes is calculated as shown in the following equation:

$$\left| \frac{F_{abs.\max.}}{F_{rel.\max.}} \right| = \left| \frac{\frac{N+1}{1}}{\sin\left(\frac{3}{2}\frac{\pi}{N+1}\right)} \right| = \left| (N+1) \sin\left(\frac{3}{2}\frac{\pi}{N+1}\right) \right| \quad (2.7)$$

For $N \rightarrow \infty$ the argument of the sin function tends to zero, so $\sin x \simeq x$.

$$\left| \frac{F_{abs.\max.}}{F_{rel.\max.}} \right| \simeq 5 \quad (2.8)$$

That is:

$$SLL = 20 \log_{10} \left| \frac{F_{abs.\max.}}{F_{rel.\max.}} \right| \simeq 14 \text{ dB} \quad (2.9)$$

For small values of N , the SLL is less than 14 dB, but it will never exceed this value without the use of nonuniform amplitude distributions, such as binomial or Chebyshev distributions, specifically designed to reduce sidelobes at the expense of a larger main lobe.

Arrays for which the maximum is orthogonal to the direction of alignment are called **broadside arrays**. In this type of array, we will have that $u_0 = 0$, so all radiating elements are in phase and the main lobe will be centred in the origin of the axes. Having the maximum at $u = u_0$ means that $u = k_o d \cos \psi = 0$, so $\psi = \frac{\pi}{2}$. For the main lobe to be unique in the visible space, the following condition must be satisfied:

$$k_0d = 2\pi - \frac{2\pi}{N+1} = 2\pi \frac{N}{N+1} \quad (2.10)$$

From which we derive that:

$$k_0d \leq 2\pi \frac{N}{N+1} \quad (2.11)$$

Substituting k_0 for $2\pi/\lambda$, we obtain:

$$\frac{2\pi}{\lambda}d \leq 2\pi \frac{N}{N+1} \implies \frac{d}{\lambda} \leq \frac{N}{N+1} \implies d \leq \lambda \frac{N}{N+1} \quad (2.12)$$

This relationship shows that the distance d between elements must be less than that value to avoid the formation of unwanted lobes. For $N \rightarrow \infty$, we arrive at the asymptotic condition for which $d \leq \lambda$, so for arrays with many elements, the spacing can be at most equal to λ to ensure that the broadside array has a single maximum in the visible space.

By setting the value of u_0 equal to $+k_0d$ or $-k_0d$ instead, we can obtain the **end-fire array**. The resulting effect is a shift of the main lobe to $\pm k_0d$.

To have $u = u_0 \implies k_0d \cos \psi = \pm k_0d \implies \psi = 0$ or $\psi = \pi$.

This indicates that the main lobe is aligned with the axis of the array, differing from the broadside array, in which the main lobe is perpendicular to the array. In this case, the condition to be satisfied for the main lobe to be unique in the visible space is:

$$k_0d \leq (-k_0d + 2\pi) - \frac{2\pi}{N+1} \implies d \leq \frac{\lambda}{2} \left(\frac{N}{N+1} \right) \quad (2.13)$$

By varying u_0 in the range $[-k_0d, k_0d]$, the main lobe moves from one semi-axis to the other, thus allowing its direction to be changed.

Binomial Array

The binomial array is a particular type of antenna array designed to achieve a radiation pattern in which the Side Lobe Magnitude is zero. This is achieved by applying nonlinear antenna tapering techniques, assigning an amplitude to the feeding currents of each antenna element, which follows the binomial coefficients. In practice, elements closer to the center receive higher currents, while those toward the outside of the array receive weaker currents, creating a smooth transition that reduces the formation of unwanted lobes.

The main advantage of this configuration is the ability to focus energy in one direction without energy losses due to the presence of side lobes. However, this solution also has disadvantages: it requires a very precise power supply and involves a greater width of the main lobe than other types of arrays. A trade-off between the width of the side lobes and the width of the main lobe is therefore necessary: this type of array is therefore suitable in contexts where the objective is to reduce interference, rather than to have an optimised angular resolution.

The array factor for an array of $N + 1$ antennas is expressed as a binomial expansion:

$$(a + b)^{2N} = \sum_{k=0}^{2N} C_k a^k b^{(2N-k)}, \quad \text{where} \quad C_k = \frac{(2N)!}{k!(2N-k)!} \quad (2.14)$$

The array factor expression for a binomial array can be written as a binomial sum:

$$F_d(u) = (e^{ju} + 1)^{2N} = \sum_{n=0}^{2N} C_n e^{jnu} \quad (2.15)$$

The C_n are the binomial coefficients, which determine the amplitude of the current in the different elements of the binomial antenna array.

The array factor has only the main lobe and not the secondary lobes. Increasing the value of N , the main lobe narrows and the derivatives of higher order in π are null. To achieve this kind of array function, the coefficients C_n , which are the amplitudes of the currents, must be set following Pascal's triangle.

Table 2.1: Pascal's Triangle to calculate the binomial coefficients

$n = 0$	1						
$n = 1$	1 1						
$n = 2$	1 2 1						
$n = 3$	1 3 3 1						
$n = 4$	1 4 6 4 1						
$n = 5$	1 5 10 10 5 1						
$n = 6$	1	6	15	20	15	6	1

Chebyshev Array

The Chebyshev array is a type of antenna array designed to achieve a constant level of SLL while keeping the main lobe as narrow as possible. This is achieved by using the Chebyshev function to determine the excitation amplitude of the array elements.

In this configuration, the array factor is represented by the Chebyshev polynomial:

$$T_n(x) = 2xT_{(n-1)}(x) - T_{(n-2)}(x) \quad (2.16)$$

with $T_0(x) = 1$ and $T_1(x) = x$. Higher-order polynomials can be calculated recursively.

The features of a Chebyshev polynomial are:

- in the region between $-1 \leq x \leq 1$ has limited values in the range $-1 \leq T_n \leq 1$
- the function diverges outside the region between $-1 \leq x \leq 1$.
- the function has as many zeros as its degree and they lie in the region between $-1 \leq x \leq 1$
- $T_n(\cos \gamma) = \cos(n\gamma)$, with $|x| \leq 1$
- $T_n(\cosh \gamma) = \cosh(n\gamma)$, with $|x| \geq 1$
- the positions of the zeros are: $x_0 = \cos(a_0) = \cos(\frac{\pi}{2n}(2m+1))$, with $m = 0, 1, \dots, n-1$

We can exploit the properties of Chebyshev polynomials to obtain very directional arrays. Defining the variable $x = a + b \cos u$, with $a, b > 0$, we can rewrite the Chebyshev polynomial as:

$$T_N(x) = \sum_{n=0}^N C_n \cos(nu) \quad (2.17)$$

Considering a symmetrical array, the previous equation can be summarized with the array factor:

$$F(u) = I_0 + 2 \sum_{n=1}^N I_n \cos(nu), \quad \text{with } I_n = \frac{C_n}{2} \quad (2.18)$$

The constants a and b can be chosen such that the visible space defined for u corresponds to the values of x in the range $-1 \leq x \leq x_1$ with $x_1 > 1$. $T_n(x_1)$ will be the maximum of $F(u)$ and will be greater than 1, while the secondary lobes will appear in the region $-1 \leq x \leq 1$ and will have the maximum value equal to 1.

We can exploit the characteristics of the Chebyshev polynomial to obtain a ratio R between the main lobe and the secondary lobes, which is equivalent to saying $T_N(x_1) = R$. From the characteristics of the Chebyshev polynomial:

$$T_n(\cos \gamma_1) = \cosh(n\gamma_1) = R, \quad \text{with } \gamma_1 = \frac{1}{n} \cosh^{-1} R \quad (2.19)$$

It follows that $x_1 = \cosh \gamma_1 = \cosh \left(\frac{1}{n} \cosh^{-1} R \right)$. The latter equation allows the system to be solved with respect to a and b .

$$\begin{cases} b = \frac{\cosh \left(\frac{1}{n} \cosh^{-1} R \right) + 1}{1 - \cos(k_0 d)} \\ a = \cosh \left(\frac{1}{n} \cosh^{-1} R \right) - b \end{cases}$$

By fixing a and b , it is possible to calculate all the C_n useful to obtain the amplitudes of the feed currents of the antenna elements of the array.

2.3 Simulation Software and Setup

MATLAB was used to develop the project, in particular the Antenna Toolbox and the Antenna Designer app, tools that allow modeling, simulation, and analysis of arrays and individual antennas. These tools facilitated the study of the electromagnetic behavior of the antennas employed, allowing analysis of S_{11} parameters, radiation pattern, impedance matching, gain, frequency response and coupling properties between antennas.

2.3.1 Patch Microstrip Parameters Optimazation

The microstrip patch antenna was optimized for a 5 GHz operating frequency via the Antenna Designer app, ensuring a constant impedance match of 50Ω (Fig. 2.1).

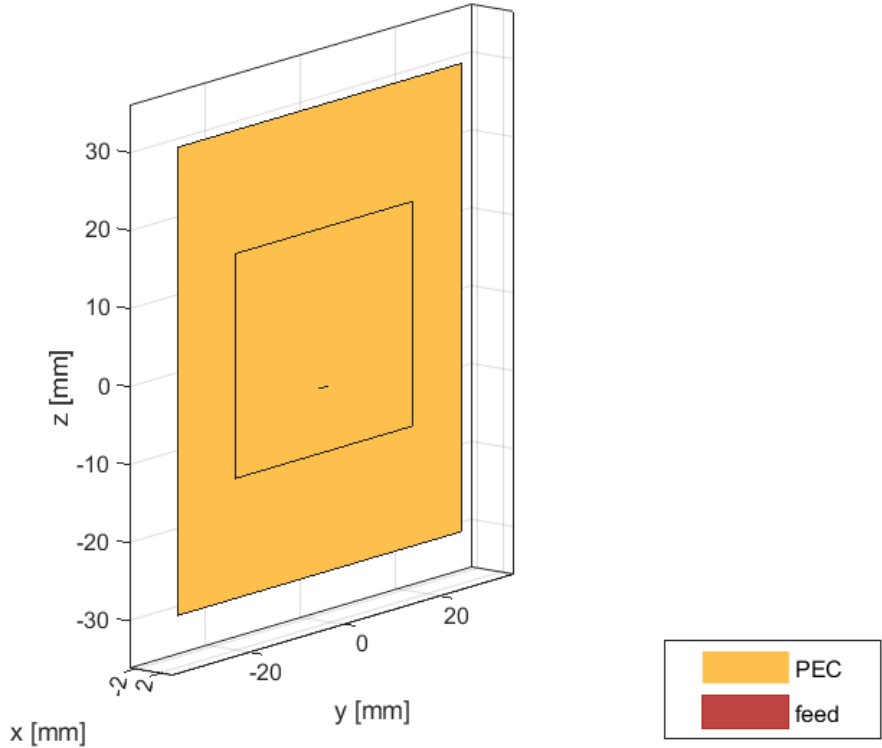


Figure 2.1: Representation of the Patch Microstrip Antenna

The geometric dimensions, shown in Tab. 2.2, include the square structure, dielectric substrate, and ground plane. The position of the feed point, defined by a specific FeedOffset, was optimized to minimize the reflection coefficient.

Table 2.2: List of the constant design parameters for patch microstrip antenna at 5 GHz

Name	Value
Length	0.02878 m
Width	0.037474 m
Height	0.00059958 m
GroundPlaneLength	0.059958 m
GroundPlaneWidth	0.059958 m
PatchCenterOffset	[0,0]
FeedOffset	[0.006059 m, 0]
Substrate	Air ($\epsilon_r = 1$)
Conductor	PEC

The results, in Fig. 2.2, demonstrate an $S_{11} < -10 \text{ dB}$ at 5 GHz, confirming efficient radiation with low losses. The compact, high-efficiency design is suitable for GHz-band applications where reliable performance and simplified integration are required.

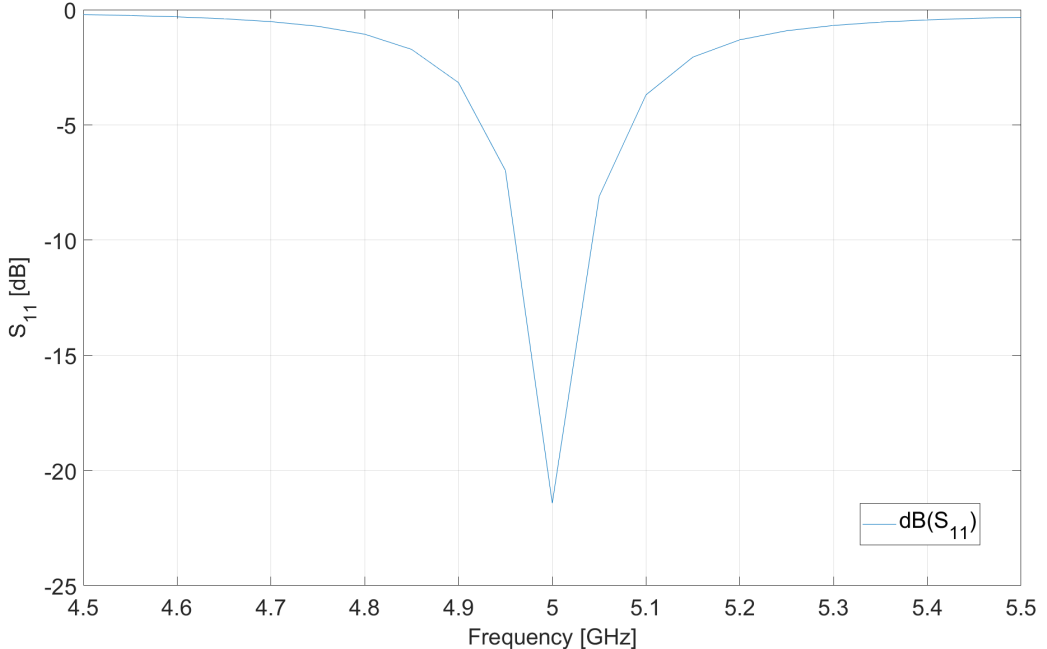


Figure 2.2: S_{11} parameter for a optimized Microstrip Patch antenna at 5 GHz

For the understanding of the spatial behavior of the microstrip patch antenna, we can analyze the 2D and 3D radiation patterns, which are essential for evaluating how the antenna radiates energy into the surrounding space and how effectively it can concentrate that energy in specific directions.

2D radiation diagrams can be of two types depending on the cut plane chosen:

- **Azimuth cut:** is the section of the radiation pattern in the xy plane. It represents the variation of gain or signal strength as a function of the azimuth angle ϕ , while

the elevation angle θ remains fixed. Generally, we set $\theta = 90^\circ$ to obtain a horizontal view of the radiation pattern, which is useful for analysing the angular coverage in the horizontal plane.

- **Elevation cut:** is the section of the radiation pattern in a vertical plane, which can be xz or yz depending on the orientation chosen. It shows the variation of gain as a function of the elevation angle θ , maintaining a fixed value for the azimuth angle ϕ . Typically one chooses $\phi = 0^\circ$ or $\phi = 90^\circ$ to obtain vertical sections describing the distribution of the signal in height with respect to the antenna, which is useful for evaluating directivity and the vertical radiation angle.

Fig. 2.3a shows the radiation pattern in the azimuth plane of a patch microstrip antenna. The diagram shows how the intensity of the radiated signal varies as a function of angle, from 0° to 360° , where the distance from the centre represents the gain in decibels. The direction of maximum radiation is along the x axis, with an amplitude of 10.08 dB , with a weaker back lobe in the opposite direction, behaving bidirectionally and symmetrically. The 3D radiation pattern is a three-dimensional graphic representation that shows how an antenna radiates or receives electromagnetic energy in all directions in space. Unlike traditional 2D diagrams (which show the azimuth and elevation planes separately), the 3D pattern offers a complete visualisation of the electromagnetic field strength (expressed in terms of gain) around the antenna, allowing one to assess the antenna's ability to concentrate energy in preferential directions compared to an isotropic radiator, regions of secondary radiation and the spatial distribution of the field and orientation of the wave. As shown in Fig. 2.3b, the 3D radiation pattern of the microstrip patch antenna, operating at 5 GHz , shows a strongly directivity behaviour along the x axis. The maximum directivity value confirms the values analysed previously. The diagram also shows the presence of a rear lobe, with a minimum directivity value of -35.3 dBi .

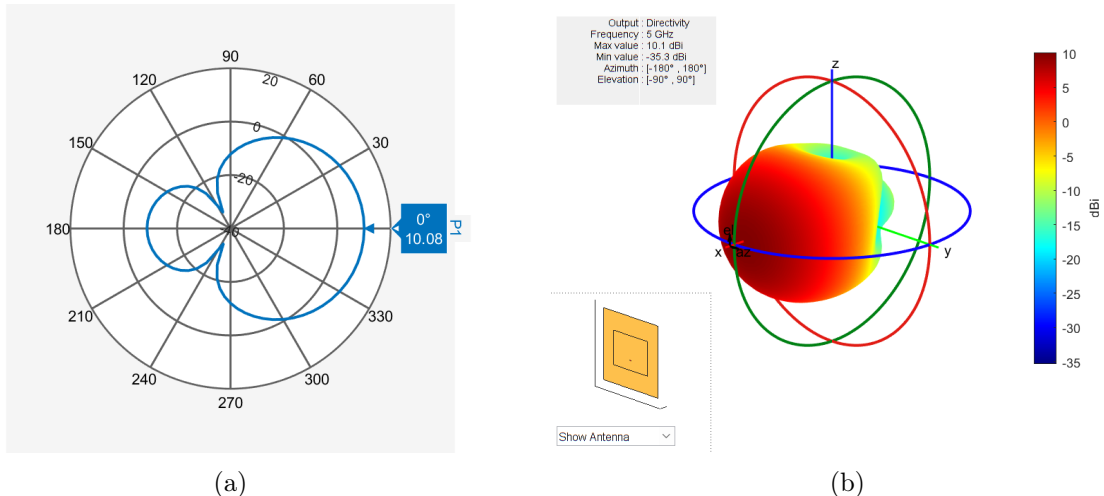


Figure 2.3: Radiation diagrams of the optimized patch microstrip antenna at 5 GHz : (a) polar radiation pattern (azimuth cut), (b) 3D radiation pattern

2.4 ULA Array

2.4.1 Number of Antenna Sweep

The objective of the analysis is to evaluate the performance of the array as the number of antenna elements varies, with particular attention to the characteristics of the main lobe, in terms of Magnitude and Width, and the secondary lobes. These quantities represent the parameters most significantly affected by the variation of the array cardinality.

Simulation

In this section, a ULA of patch microstrip antennas is analyzed, the parameters of which are shown in Tab. 2.3. As can be seen, the antennas are all fed with the same current amplitude I , the phase shift $\Delta\varphi$ is zero, and they are equidistant by a value of d . The number of antenna elements considered varies in a range from 3 to 20, aligned along the y axis so as to have the direction of maximum radiation on the x axis, thus obtaining a broadside array.

Table 2.3: List of the design parameters of ULA at 5 GHz with variable N

Name	Expression	Value	Description
f	-	$5 \cdot 10^9 \text{ Hz}$	Frequency
c	-	$3 \cdot 10^8 \text{ m/s}$	Speed of Light
I	-	1 mA	Current
λ	c/f	60 mm	Wavelength
d	$\lambda/2$	30 mm	Antenna Elements Spacing
N	-	$3 \div 20$	Number of Antenna Elements
$\Delta\varphi$	-	0°	Phase Shift

In Fig. 2.4 and 2.5 are shown, respectively, the 3D and 2D radiation patterns (azimuth cut) of two antenna arrays, with 5 elements (2.4a, 2.5a) and 15 elements (2.4b, 2.5b). The array with $N = 5$ presents a radiation pattern characterized by a relatively wide main lobe in the horizontal plane, oriented along the x axis, with side lobes of relatively high amplitude, a maximum gain of 15.08 dB and a main lobe width of 19.9°. This configuration, typical of arrays with few elements, provides wider coverage but with less magnitude and parasitic lobe control.

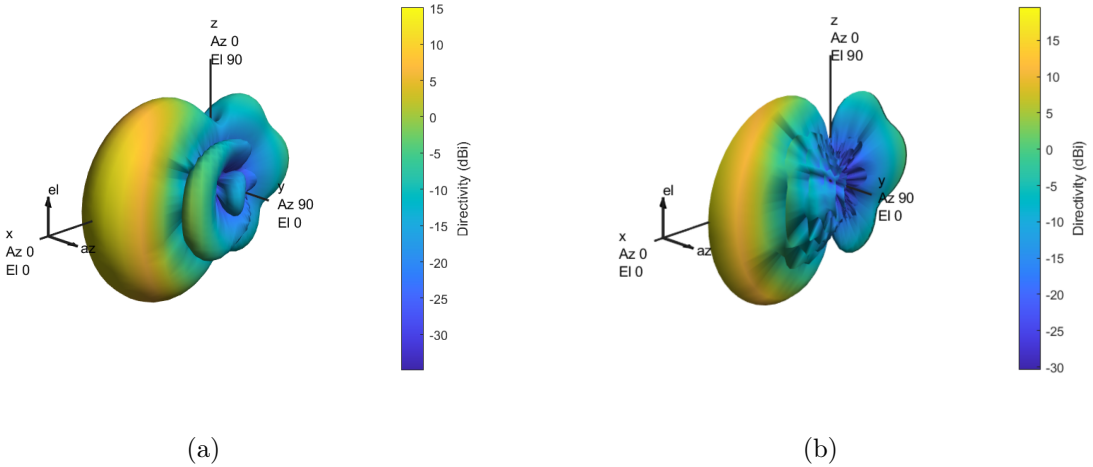


Figure 2.4: 3D radiation pattern at 5 GHz for ULA of Patch Microstrip Antennas: (a) $N = 5$, (b) $N = 15$

The array with $N = 15$, on the other hand, exhibits more direct and focused behavior. The main lobe in the horizontal plane is much narrower ($\text{HPBW} = 7.98^\circ$), with maximum gain reaching 19.6 dB and the first secondary lobes attenuated to about 6 dB .

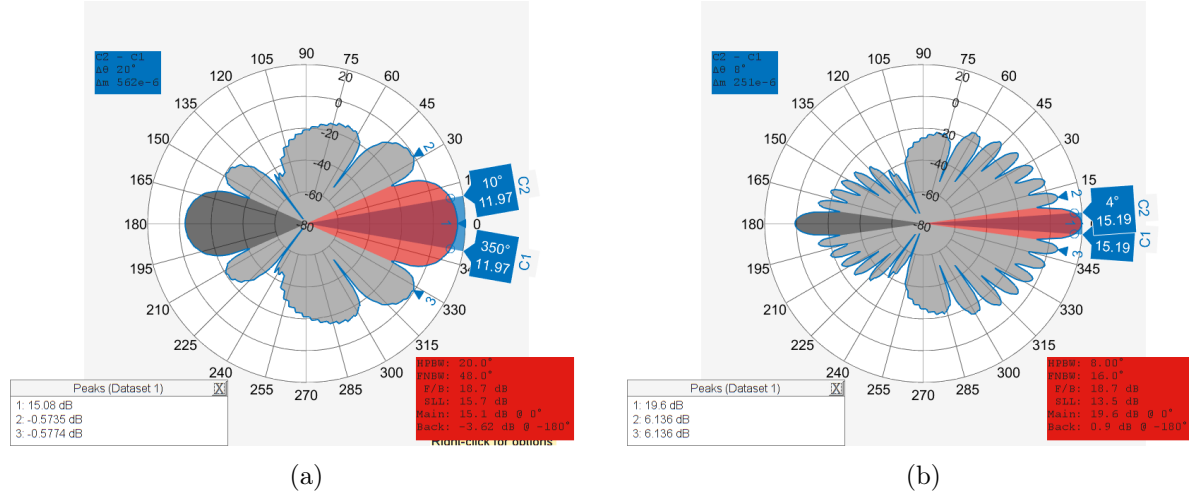


Figure 2.5: Polar radiation pattern at 5 GHz for ULA of Patch Microstrip Antennas: (a) $N = 5$, (b) $N = 15$

Increasing N allows for a narrower beam, higher gain and better control of side emissions, at the expense of greater system complexity due to the larger number of antenna elements.

Results

We will now analyze the various parameters of interest as a function of the number of antenna elements, namely:

- Main Lobe Magnitude: maximum intensity of the main lobe, measured in dB ;
- Main Lobe Width (HPBW): angular width measured on the main lobe at half-power;
- Main Lobe Direction: pointing angle of maximum radiation;
- Side Lobe Magnitude: intensity of side lobes in dB ;
- Side Lobe Level (SLL): ratio in dB between main lobe and highest side lobe.

As shown in Fig. 2.6 by increasing the number of antenna elements from 3 to 20, the magnitude of the main lobe increases, reaching a peak of about 20 dB . The ULA thus allows, by increasing the number of antennas, to increase the maximum magnitude of the main lobe.

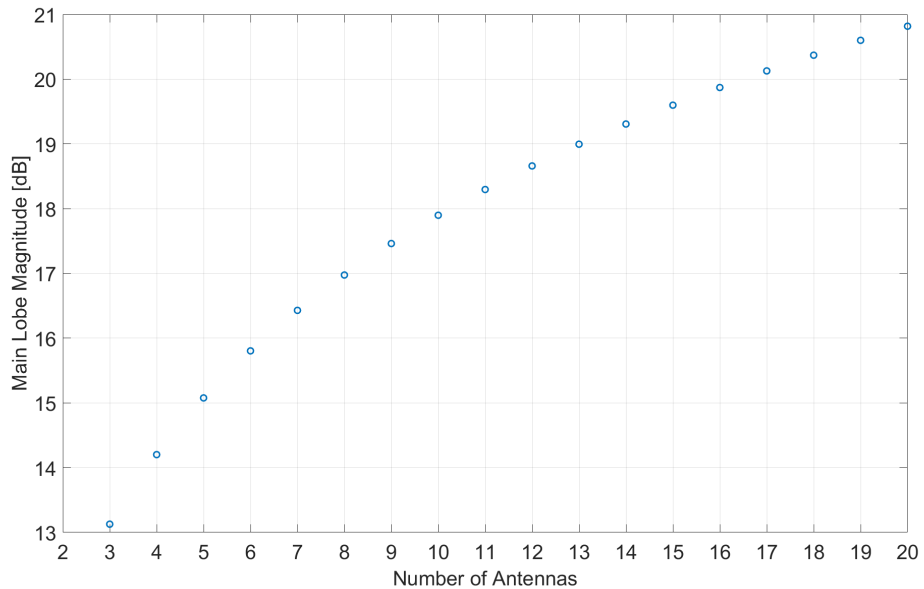


Figure 2.6: Main Lobe Magnitude as a function of number of antenna elements N for ULA of Patch Microstrip Antennas at 5 GHz

Fig. 2.7 shows the trend of Main Lobe Magnitude (HPBW) as a function of the number of elements in the array. Unlike main lobe magnitude, which increases with the number of antennas, HPBW exhibits an inversely proportional behavior: as the number of elements increases, there is a progressive reduction in the width of the main lobe. This shows how larger arrays produce more directional radiation patterns, concentrating energy in a narrower beam and consequently improving the angular resolution of the system. We start at 33° width when the array is made up of 3 antennas, until we get to 6° when there are 20 antennas. The trend shows also that, after 17 antennas, the width seems not to improve, due to the physical limits of this configuration.

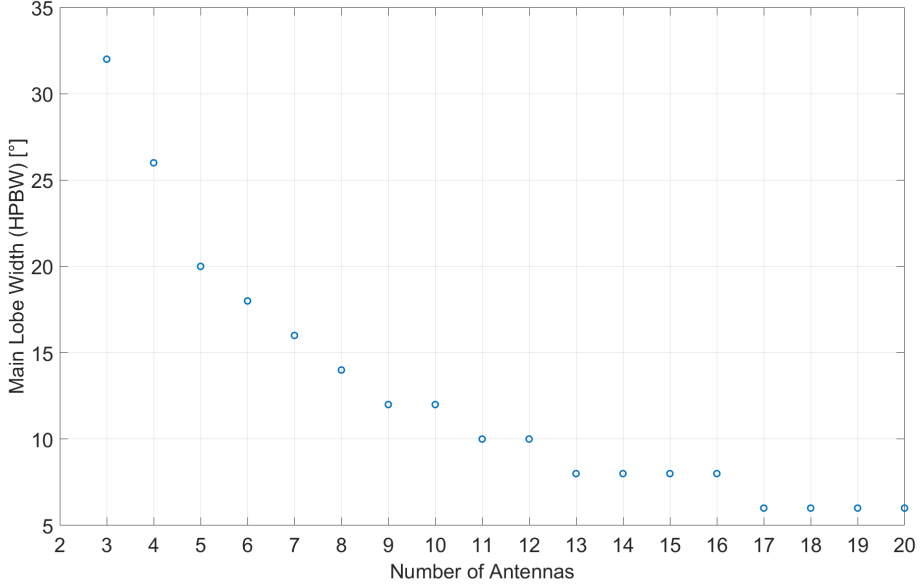


Figure 2.7: Main Lobe Width as a function of number of antenna elements N for ULA of Patch Microstrip Antennas at 5 GHz

As evidenced in Fig. 2.8, the absence of phase shift ($\Delta\varphi$) guarantees a constant maximum radiation direction on the azimuth plane at $\phi = 0^\circ$, regardless of array size. This experimental result confirms the theoretical principle that, under uniform feeding conditions between antenna elements, the direction of the main lobe in a ULA remains unchanged as the number of N elements varies.

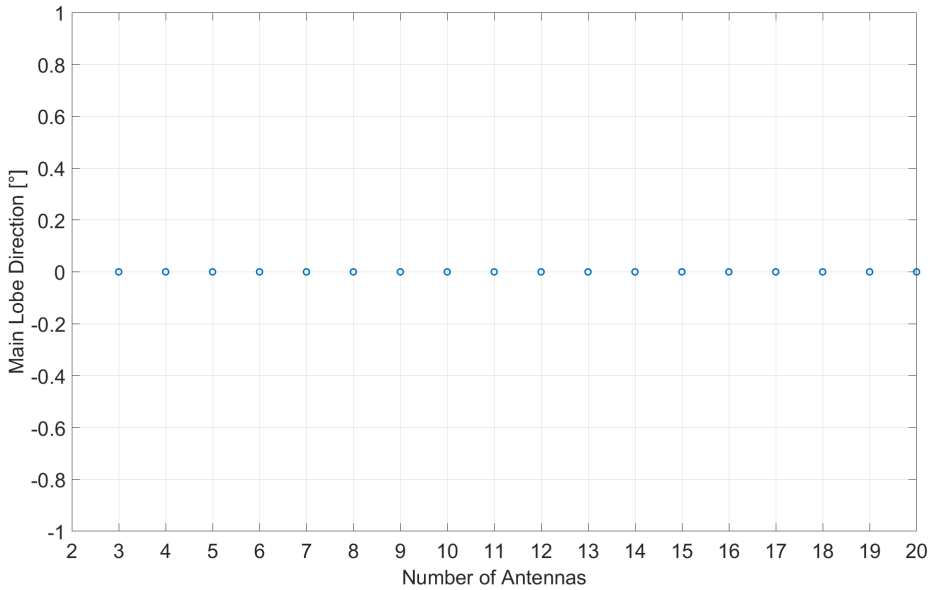


Figure 2.8: Main Lobe Direction as a function of number of antenna elements N for ULA of Patch Microstrip Antennas at 5 GHz

Fig. 2.9 shows how the side lobe magnitude follows an increasing trend similar to that of the main lobe, increasing proportionally to the number of antenna elements. This behavior highlights an inherent limitation of ULA configurations: although array gain improves with more elements, effective suppression of side lobes cannot be achieved, regardless of

array size. With only 3 antennas, the magnitude is -8 dB , reaching almost 8 dB with the higher number of antennas considered.

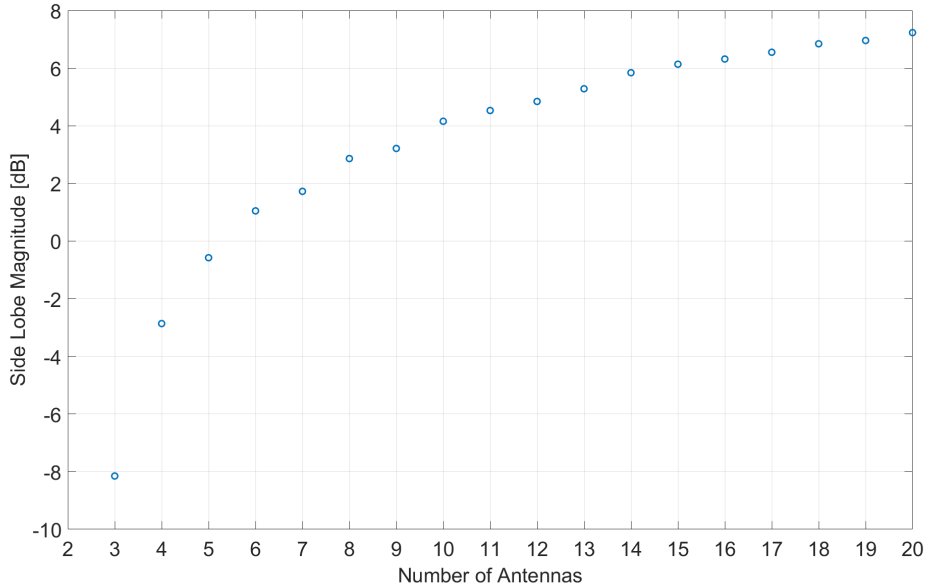


Figure 2.9: Side Lobe Magnitude as a function of number of antenna elements N for ULA of Patch Microstrip Antennas at 5 GHz

Confirming what has been said about the Side Lobe Magnitude, we can observe Fig. 2.10, which shows that the SLL decreases by increasing the number of antennas, but having arrived at about 10 antenna elements, there is no significant improvement in the parameter. which remains around 14 dB . To obtain improvements from this point of view, other solutions, such as the Binomial Array or the Chebyshev array, must be adopted.

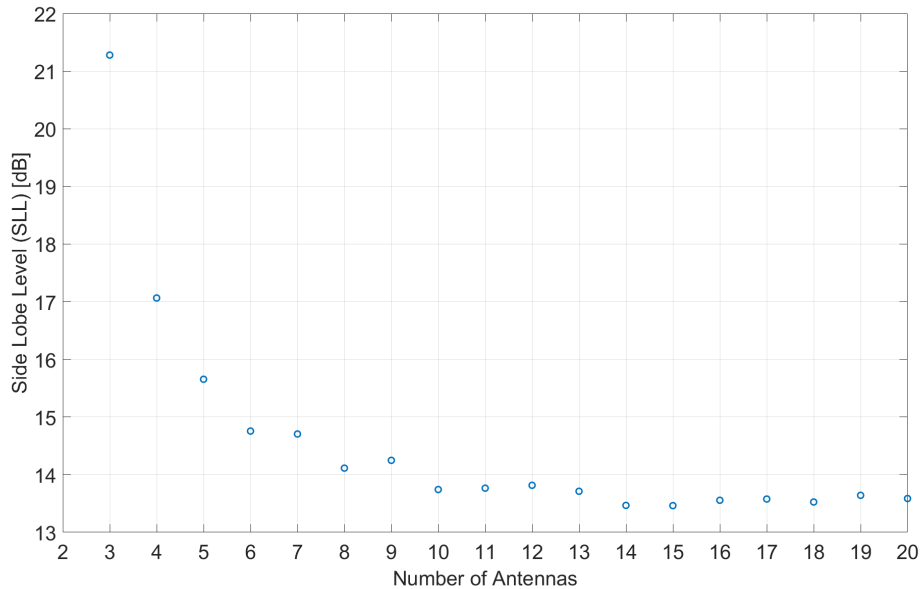


Figure 2.10: Side Lobe Level as a function of number of antenna elements N for ULA of Patch Microstrip Antennas at 5 GHz

2.4.2 Phase Shift Sweep

The objective of this analysis is to evaluate the performance of the linear array by means of a phase variation of the feed currents, while keeping the number of N antenna elements fixed at 15. The same parameters were evaluated as in the previous case, but paying more attention to the direction of the lobes, which is strongly influenced by the phase variation of the current between the elements.

Simulation

Considering Tab. 2.4, we observe how the number of radiating elements is kept constant, fixed at $N = 15$. Unlike the previous analysis, in which we varied the number of antenna elements, in this study the effect of the phase shift of the feed current between the elements is investigated, while keeping its amplitude constant. In particular, the phase shift $\Delta\varphi$ between adjacent elements is varied in a range between -180° and 180° . This configuration allows beam steering, i.e. the shifting of the main lobe of the radiation pattern along different angular directions, without physically changing the array or the intensity of the feed current.

Table 2.4: List of the design parameters of ULA at 5 GHz with phase shift

Name	Expression	Value	Description
N	-	15	Number of Antenna Elements
$\Delta\varphi$	-	$-180^\circ \div 180^\circ$	Phase Shift

In Fig. 2.11 we find the 3D radiation diagrams of the ULA composed of 15 antenna elements, analysed for three different phase shift values between adjacent elements.

For $\Delta\varphi = -90^\circ$ (Fig. 2.11a) the main lobe is deflected with respect to the x axis, confirming the effect of beam steering introduced by the negative -90° phase. However, the side lobes have a relatively high magnitude, which then results in a loss of energy in unwanted directions.

On the other hand, for $\Delta\varphi = +45^\circ$ (Fig. 2.11b), a less inclined orientation of the main lobe is observed compared to the previous case. The pattern maintains good symmetry and an even directivity distribution, with a still well-focused beam and secondary lobes that are more contained with respect to the previous case.

Finally, for $\Delta\varphi = -180^\circ$ (Fig. 2.11c) a much more complex pattern is evident in this case, with the appearance of numerous secondary lobes and a deterioration of the main directivity. The high phase shift introduced between the elements results in a significant dispersion of the energy over a wider angular area, which translates into a decreased ability to concentrate the beam. This time, the maximum of the radiation can be found on the alignment axis of the array, thus has become an end-fire array.

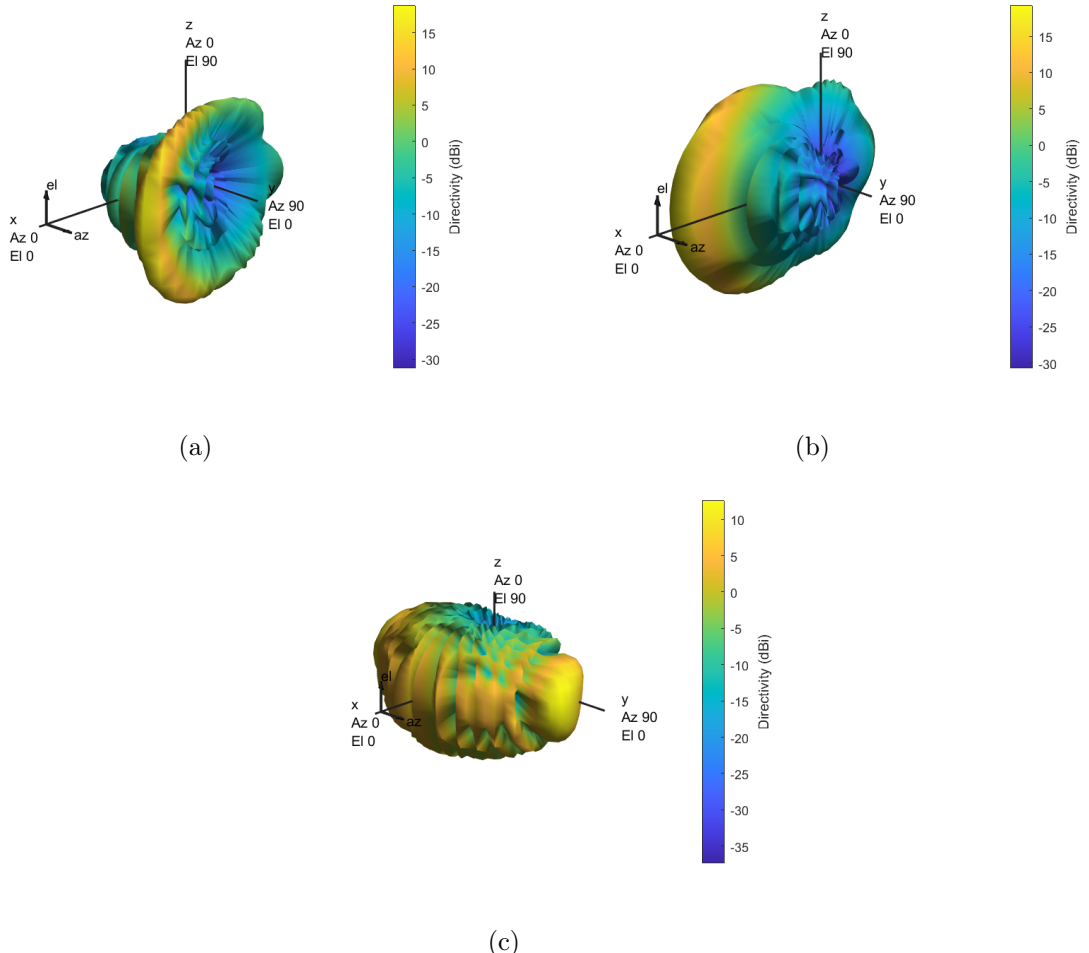


Figure 2.11: 3D radiation pattern at 5 GHz for ULA of Patch Microstrip Antenna with $N = 15$ for different phase shift: (a) $\Delta\varphi = -90^\circ$, (b) $\Delta\varphi = +45^\circ$, (c) $\Delta\varphi = -180^\circ$

Fig. 2.12 shows the polar radiation patterns (azimuth cut) as the phase shift $\Delta\varphi$ between the elements varies. These graphs confirm the results already analysed in the case of the 3D radiation diagrams.

In the case in Fig. 2.12a, with a phase shift $\Delta\varphi = -90^\circ$, the diagram shows a main lobe directed around about 30° , with a maximum gain of about 18.76 dB . Two secondary lobes of lesser intensity are also observed, around 7.23 dB and 3.88 dB respectively, but negatively affecting the antenna performance, as anticipated in the respective 3D pattern analysis;

In the case in Fig. 2.12b, with $\Delta\varphi = +45^\circ$, the main lobe is oriented around about -15° , with a slightly higher maximum gain (19.3 dB), indicating greater directivity than in the previous case. Side lobes are also present in this scenario, with intensities of 6.77 dB and 4.91 dB , but the magnitude of the other side lobes is reduced compared to the previous case, due to the fact that we are using a smaller shift;

Finally, the case in Fig. 2.12c, with $\Delta\varphi = -180^\circ$, shows a markedly different behaviour, with the main lobe being directed towards 72° , but the maximum gain is significantly reduced (about 13.43 dB), in favour of more pronounced side lobes in the xy plane.

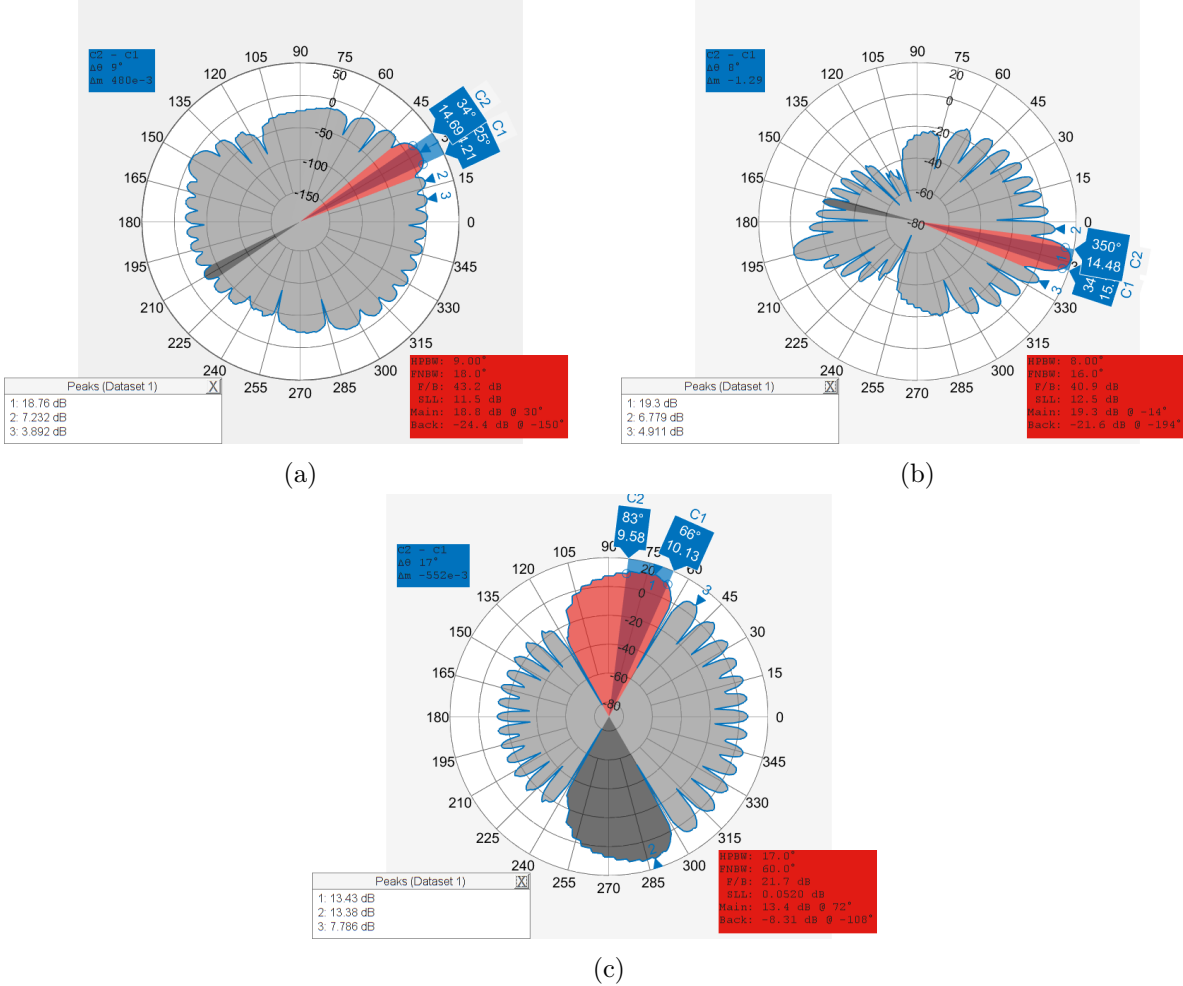


Figure 2.12: Polar radiation pattern at 5 GHz for ULA of Patch Microstrip Antenna with $N = 15$ for different phase shift: (a) $\Delta\varphi = -90^\circ$, (b) $\Delta\varphi = +45^\circ$, (c) $\Delta\varphi = -180^\circ$

Results

It is now possible to evaluate the same parameters analysed in the previous case but considering the phase shift $\Delta\varphi$.

As we can observe in Fig. 2.13, the Main Lobe Magnitude decreases the more we deviate from the case where there is no phase shift between the feeds of the antenna elements: there is in fact for $\Delta\varphi = 0^\circ$, the maximum of the constructive interference along the x -axis and thus the respective maximum of the magnitude of almost 20 dB in the broadside direction. When we consider instead the $\Delta\varphi = 180^\circ$, as seen before, the array becomes end-fire, with a higher percentage of power distributed over the side lobes, resulting in a smaller main lobe magnitude, of about 13 dB.

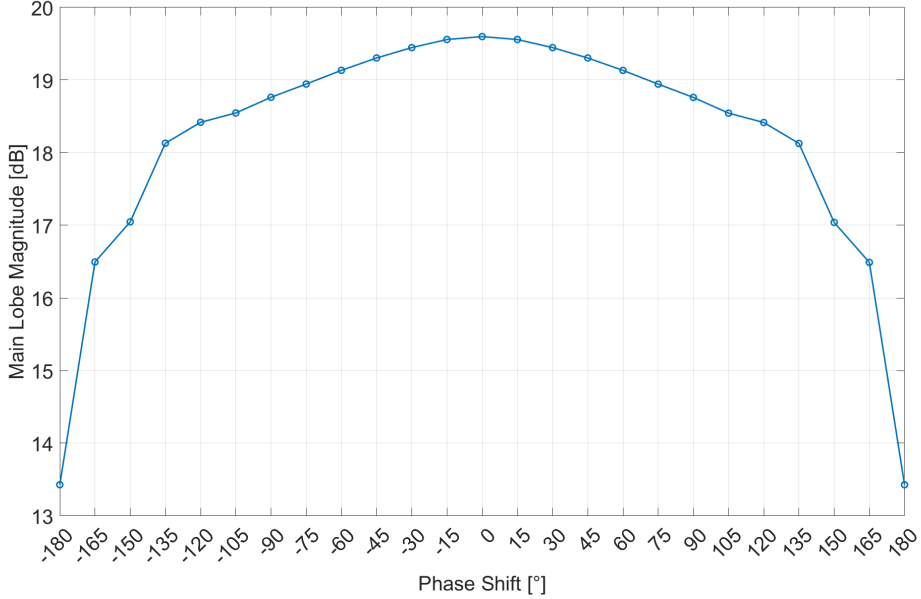


Figure 2.13: Main Lobe Magnitude as a function of phase shift $\Delta\varphi$ for ULA of $N = 15$ Patch Microstrip Antennas at 5 GHz

For the Main Lobe Width in Fig. 2.14, we observe that the width is minimised when we have no phase shift, whereas at $\pm 180^\circ$ shifts, the main lobe is much wider, as also shown earlier in the radiation patterns. The starting point at $\Delta\varphi = 0^\circ$ shows a width of only 8° , against a width of 17° when we hit a phase shift of $\Delta\varphi = 180^\circ$

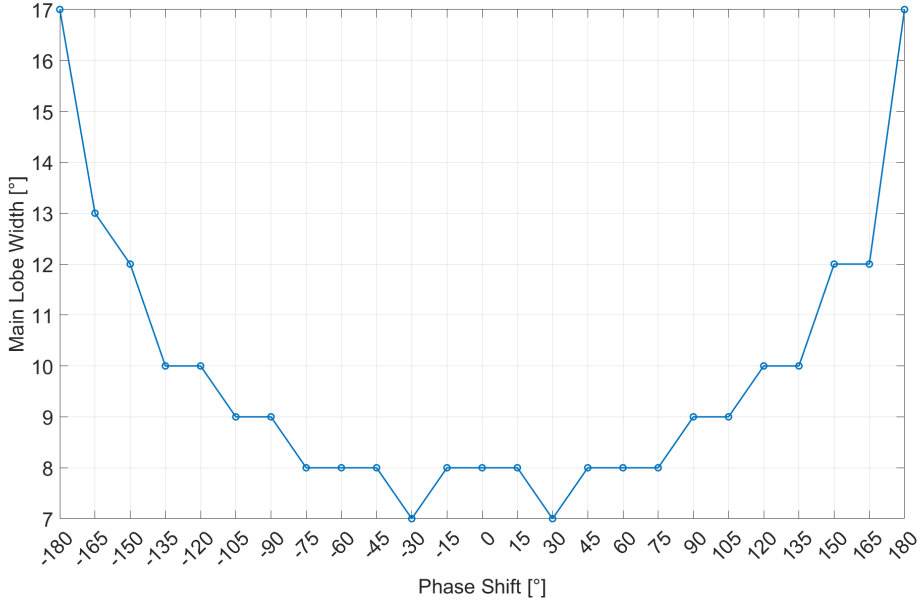


Figure 2.14: Main Lobe Width as a function of phase shift $\Delta\varphi$ for ULA of $N = 15$ Patch Microstrip Antennas at 5 GHz

In Fig. 2.15, we compare the Main Lobe Direction with respect to the azimuth angle. This is the main reason for the usage of a different phase shift for the currents, thanks to which we can perform beamsteering. When $\Delta\varphi = 0^\circ$, the direction of the main lobe is broadside, i.e. in the direction of the x -axis, orthogonal to the array's alignment. Increasing the phase shift, in particular at $\Delta\varphi = \pm 180^\circ$, the main lobe moves towards

the y axis, thus transforming the array into an end-fire array, with a marked presence of side lobes, to a greater extent than with phase shifts of lesser magnitude.

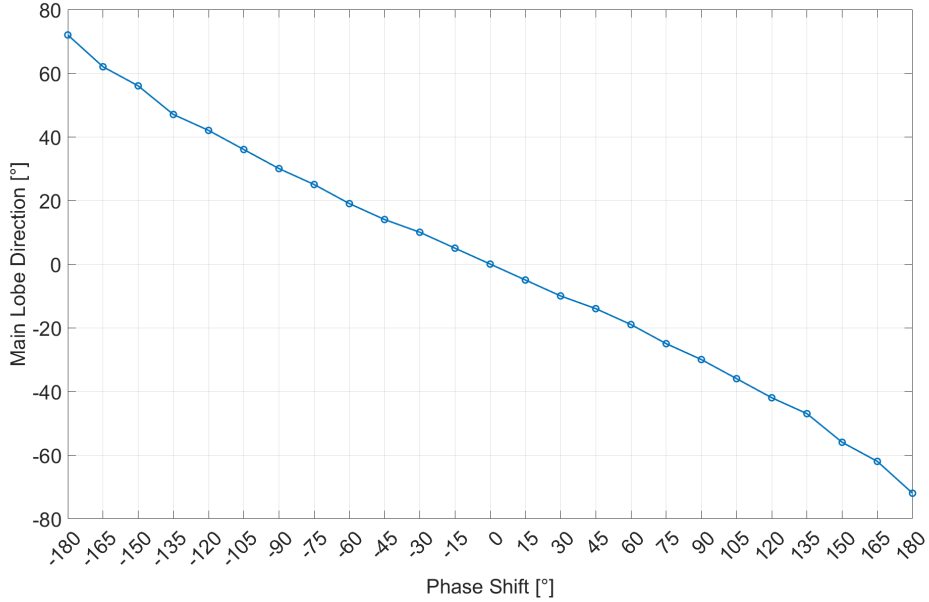


Figure 2.15: Main Lobe Direction as a function of phase shift $\Delta\varphi$ for ULA of $N = 15$ Patch Microstrip Antennas at 5 GHz

Evaluating the Side Lobe Magnitude in Fig. 2.16, we see that in the central region with phase shifts contained within $\Delta\varphi = 60^\circ$, the side lobes do not have as high a magnitude as the side lobes we find once they cross the 60° threshold. In fact, extreme values such as $\Delta\varphi = \pm 180^\circ$, tend to worsen the pattern by generating more intense side lobes, with a magnitude that reaches 8 dB, while moderate phase shifts allow for better suppression, making the pattern more direct and clean, with a magnitude between 3 dB and 6 dB.

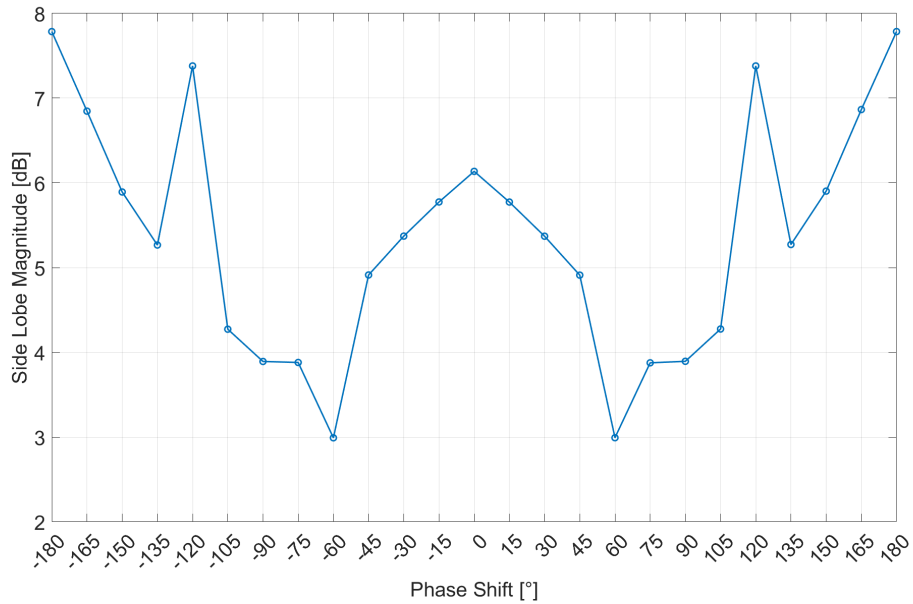


Figure 2.16: Side Lobe Magnitude as a function of phase shift $\Delta\varphi$ for ULA of $N = 15$ Patch Microstrip Antennas at 5 GHz

The graph in Fig. 2.17 shows how the Side Lobe Level depends on the phase shift applied to the array. In particular, the highest values are recorded for intermediate phase shifts (around $\Delta\varphi = \pm 60^\circ$), while the lowest values are obtained for $\Delta\varphi = \pm 180^\circ$, in correspondence with an end-fire configuration, since the Side Lobe Magnitude is higher at those points and consequently the SLL is lower. For example we can compare the SLL when the $\Delta\varphi = 60^\circ$ and $\Delta\varphi = 165^\circ$: in the first case, the SLL is equal to 16 dB, that means that we have a lower side lobe magnitude of the side lobes for that phase shift, while in the other case the SLL reaches about 10 dB, corresponding to an higher magnitude for the side lobes.

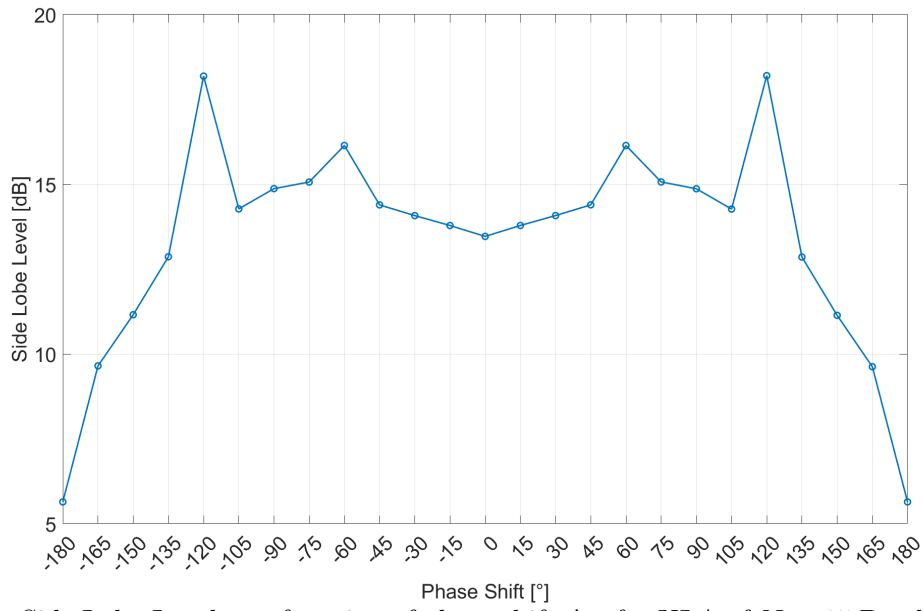


Figure 2.17: Side Lobe Level as a function of phase shift $\Delta\varphi$ for ULA of $N = 15$ Patch Microstrip Antennas at 5 GHz

2.5 Binomial Array

In this further analysis, the performance of a binomial array of microstrip patch antennas was evaluated as the number of elements in it varied. The main characteristic of the binomial distribution is its ability to effectively suppress the secondary lobes, due to the application of amplitude tapering to the intensities of the currents, based on Pascal's triangle coefficients.

2.5.1 Simulation

As in the basic ULA case, the number of antenna elements was varied between 3 and 20. In order to analyze the behavior of the binomial configuration, we will evaluate the 3D and polar patterns of the arrays composed of $N = 5$ and $N = 15$ antennas, respectively.

In Fig. 2.18a and Fig. 2.19a, the behavior of the binomial array composed of $N = 5$ patch microstrip antennas can be observed using the 3D radiation pattern. As predicted by theory, there is a reduction of the side lobes to -245.6 dB , thus allowing them to be considered as if they were absent, since their magnitude, compared to the main lobe which has a peak of 13.7 dB , turns out to be many orders of magnitude lower. On the one hand, there are no unwanted lobes and energy losses due to them, but at the price of a HPBW of 28° .

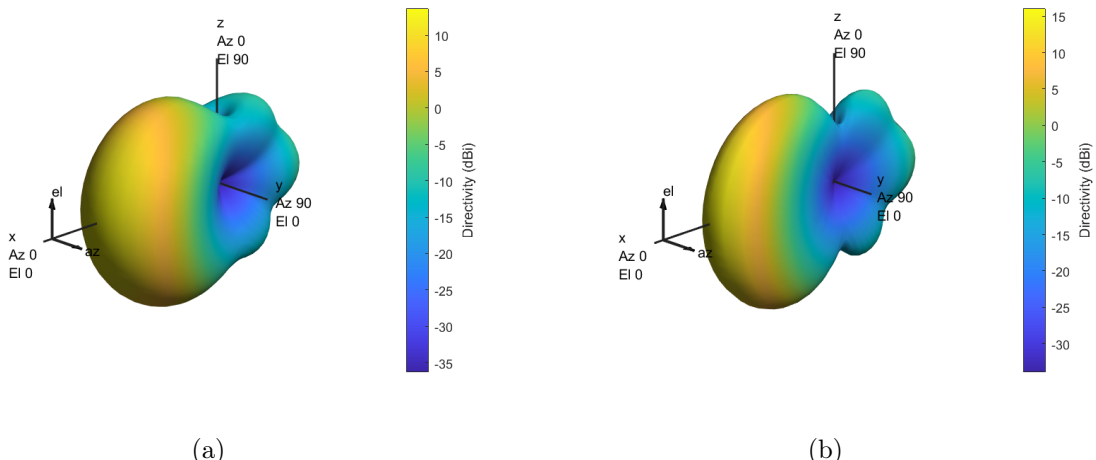


Figure 2.18: 3D radiation pattern at 5 GHz for Binomial Array of Patch Microstrip Antennas:
(a) $N = 5$, (b) $N = 15$

In Fig. 2.18b and Fig. 2.19b instead, we evaluate the performance of the binomial array composed of $N=15$ antenna elements. The array is broadside as in the previous case, thus with the maximum radiation in the x axis direction. The side lobes are further reduced (-329 dB), so they can still be considered negligible. The advantage obtained lies mainly in the main lobe magnitude and main lobe width: indeed, a narrower beam with a HPBW of 16° and an increased gain of 3 dB is observed with respect to the previous case, due to constructive interference in the broadside direction, with a maximum of 16.09 dB .

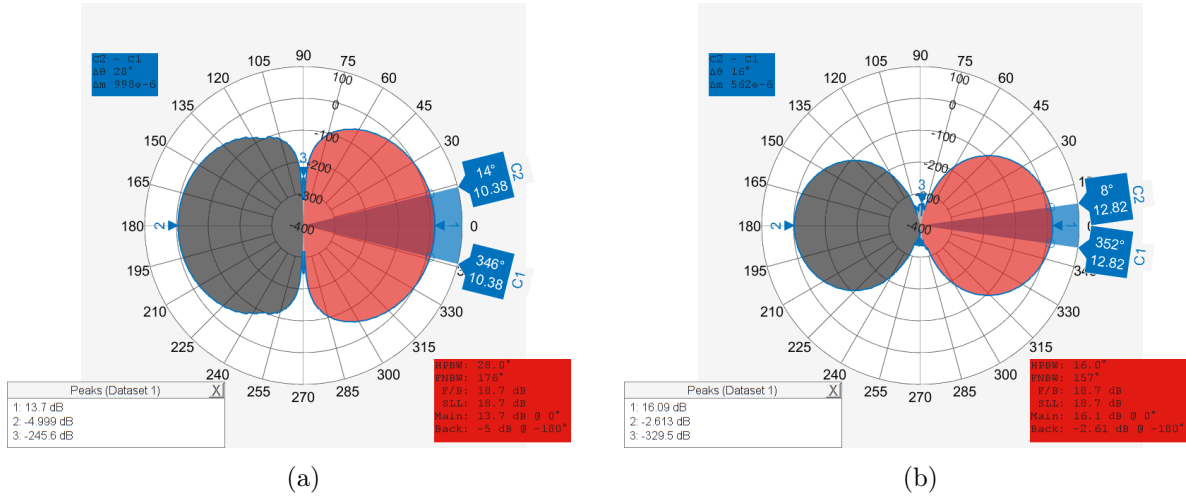


Figure 2.19: Polar radiation pattern at 5 GHz for Binomial Array of Patch Microstrip Antennas:
 (a) $N = 5$, (b) $N = 15$

2.5.2 Results

The graph in Fig. 2.20 represents the trend of the Main Lobe Magnitude as the number of N elements of the binomial array changes. Increasing the number of antennas from 3 to 20 results in a gradual increase in directivity, with values rising from about 12.6 dB to over 16.7 dB. This confirms the fact that increasing the number of elements allows more energy to be concentrated in the main beam direction, thus improving radiation efficiency.

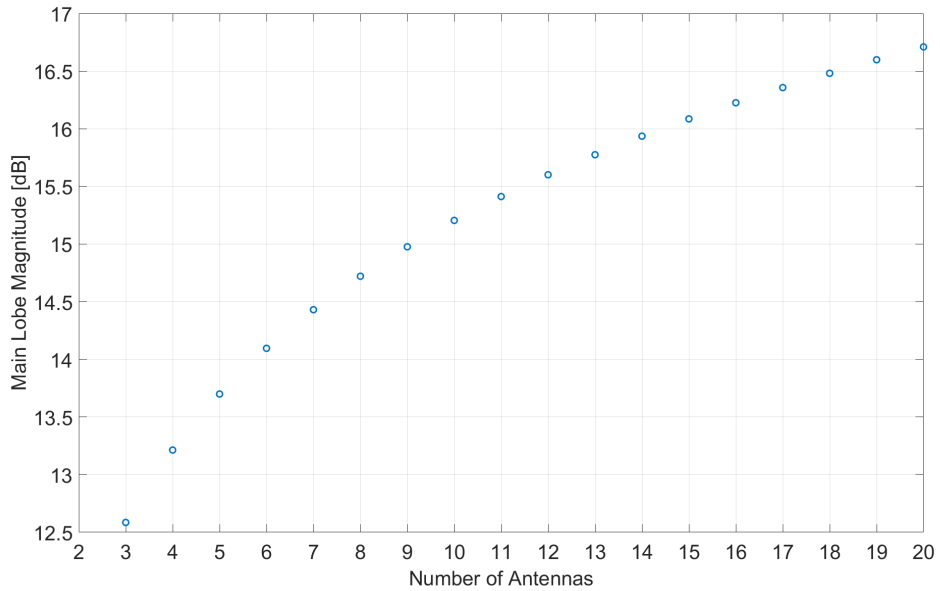


Figure 2.20: Main Lobe Magnitude as a function of number of antenna elements N for Binomial Array of Patch Microstrip Antennas at 5 GHz

In Fig. 2.21 it can be seen that the HPBW as the number of elements changes follows a decreasing trend: as the number of antennas increases, the beamwidth narrows progressively, as confirmed by the previous comparison of binomial arrays composed of $N = 5$ and $N = 15$ antennas, respectively. We go from an HPBW of about 36° for 3 antennas,

to values below 15° for 20 antennas, with less energy dispersion in unwanted directions.

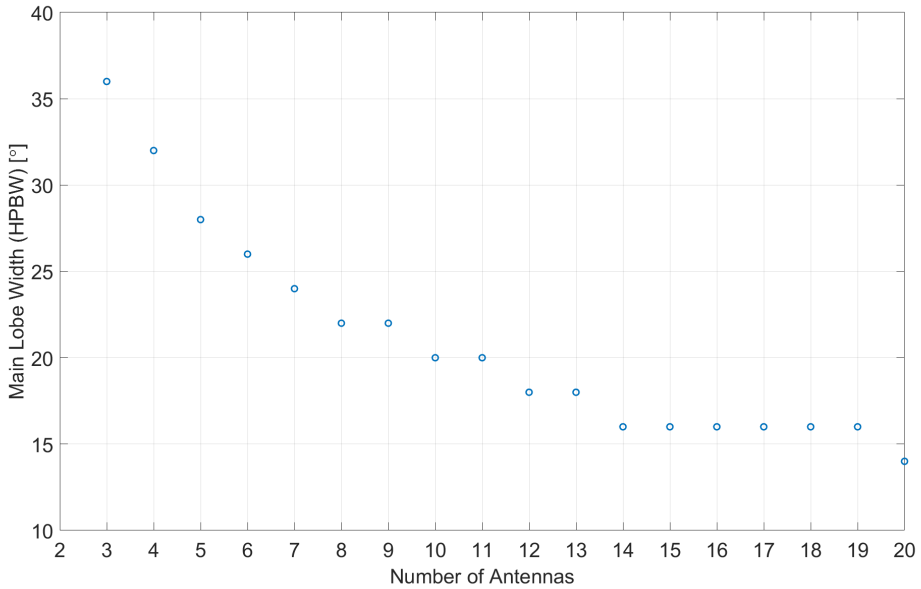


Figure 2.21: Main Lobe Width as a function of number of antenna elements N for Binomial Array of Patch Microstrip Antennas at 5 GHz

Regarding the Main Lobe Direction in Fig. 2.22, as the number of antennas increases from 3 to 20, the direction of the main beam remains essentially unchanged, thus in the broadside direction. This occurs because the $\Delta\varphi$ of the currents has not been varied between them, hence beamsteering is not achieved.

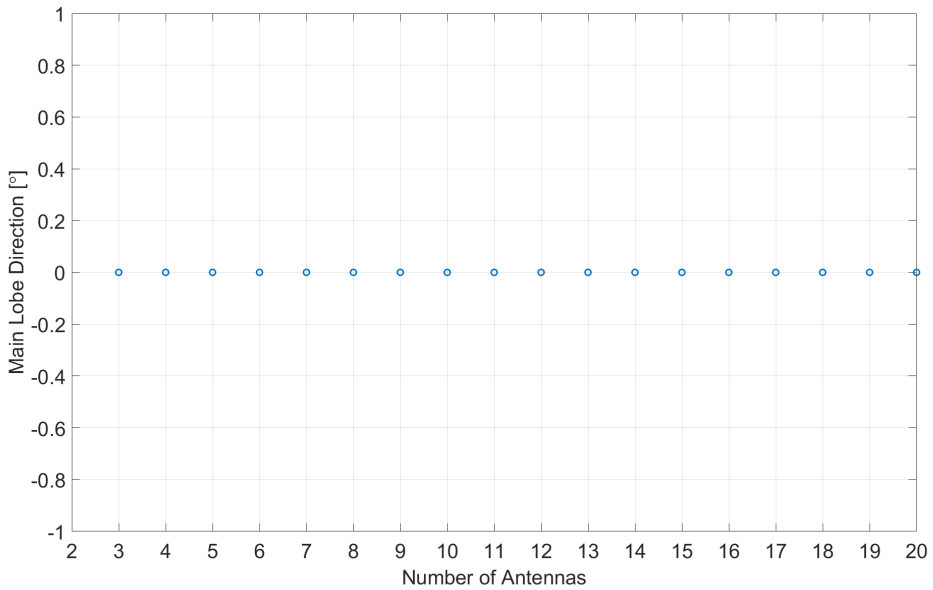


Figure 2.22: Main Lobe Direction as a function of number of antenna elements N for Binomial Array of Patch Microstrip Antennas at 5 GHz

Particularly relevant is the Side Lobe Magnitude, in Fig. 2.23, for the binomial array: in fact, even having few antenna elements, it turns out to be a very small value and therefore its effects are negligible on the overall radiation pattern and, once we get to $N = 7$, the magnitude value stabilizes around -340 dB.

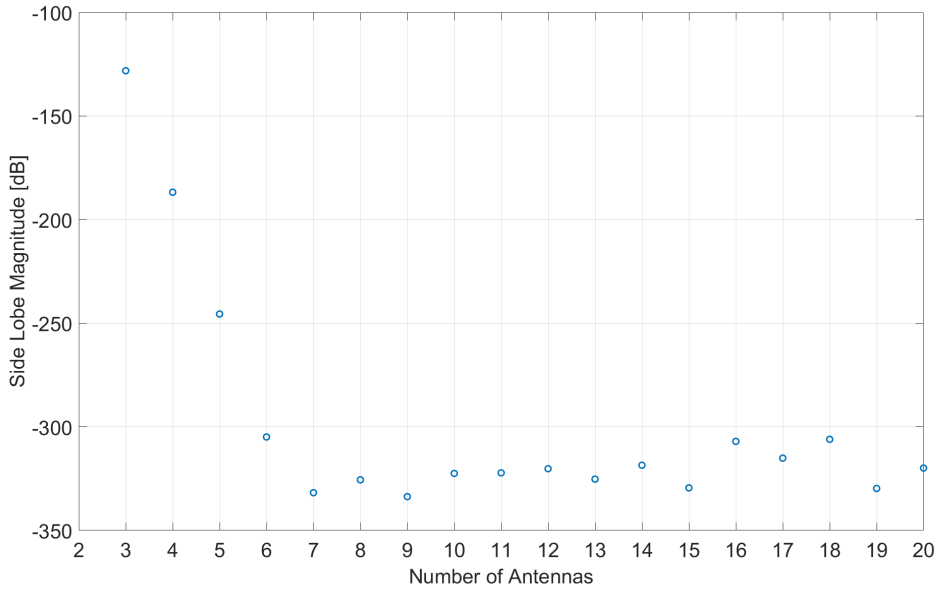


Figure 2.23: Side Lobe Magnitude as a function of number of antenna elements N for Binomial Array of Patch Microstrip Antennas at 5 GHz

In Fig. 2.24, the SLL confirms the side lobe magnitude values, increasing proportionally with the number of antennas.

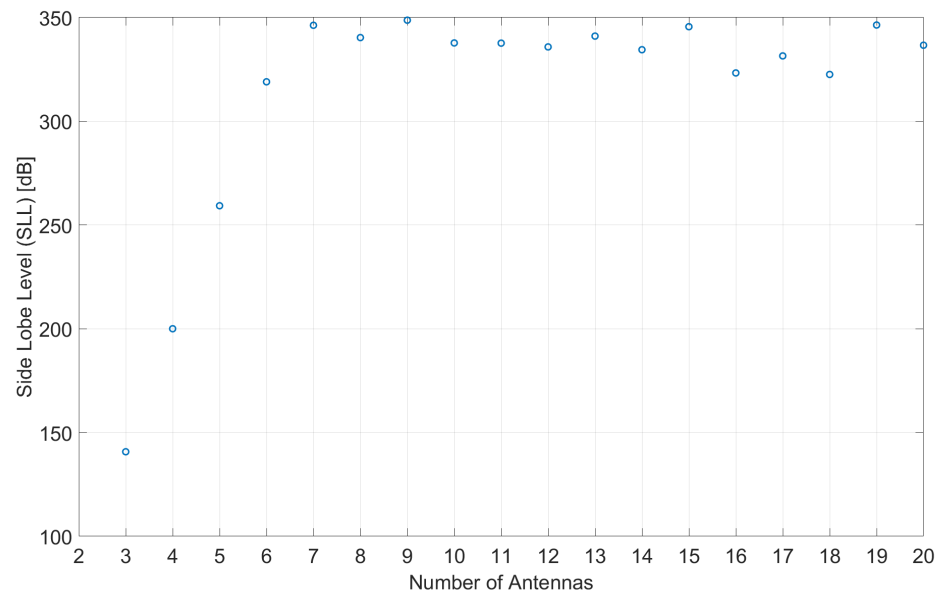


Figure 2.24: Side Lobe Level as a function of number of antenna elements N for Binomial Array of Patch Microstrip Antennas at 5 GHz

2.6 Chebyshev Array

This analysis focuses on the performance of a Chebyshev array of microstrip patch antennas as the number of antennas varies. The distinguishing feature of the Chebyshev array is its ability to precisely control the side lobe level, keeping all side lobes at the same predefined amplitude, through the use of Chebyshev polynomials for the design of current amplitude tapering. To verify this property, the goal is to set an SLL equal to 50 dB between main lobe and side lobes and evaluate the results.

2.6.1 Simulation

Fig. 2.25a shows the 3D radiation pattern of the Chebyshev array, when we choose to use a number of microstrip patches equal to $N = 5$. In this case, the pattern shows a main lobe along the x axis, thus in the broadside direction, which, however, still has a relatively large width and results in energy dissipation.

To best evaluate the distribution of the side lobes, let us make use of the polar pattern in Fig. 2.26a: we observe that the SLL stands at about 69 dB compared to the expected value of 50 dB. This occurs because we are not using a dipole antenna, whose pattern in the azimuth plane would ideally be omnidirectional, bringing the overall radiation pattern to coincide with the array factor, designed to have a constant SLL at 50 dB. However, using a microstrip patch as an element, its 3D pattern is not constant: multiplying it by the array factor results in a deformation as a result of the envelope. In this case, the result of the product between array factor and the radiation pattern of the individual element will lead to a change in the magnitude of the sidelobes, and an SLL that is at least as large as expected.

As for the amplitude of the main beam, it still turns out to be large, so let us consider the behavior of the array when the number of antennas N increases.

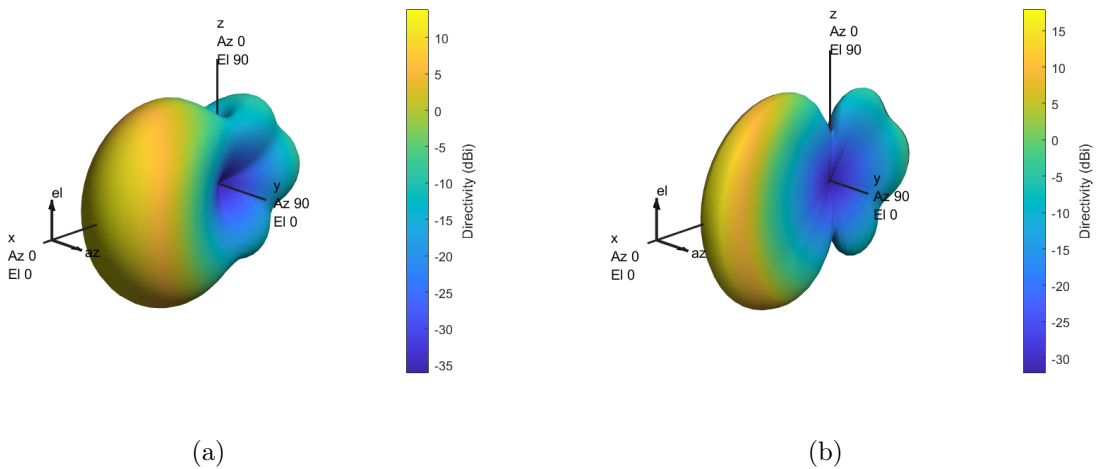


Figure 2.25: 3D radiation pattern at 5 GHz for Chebyshev Array of Patch Microstrip Antennas: (a) $N = 5$, (b) $N = 15$

For $N = 15$, the 3D pattern in Fig. 2.25b shows a significant narrowing of the main lobe, confirmed by the polar plot in Fig. 2.26b where a width of 12° is observed, compared with 26° in the previous case.

In this configuration, the SLL stabilizes around 50 dB, approaching the specified design value, unlike the $N = 5$ case where the SLL reached almost 70 dB.

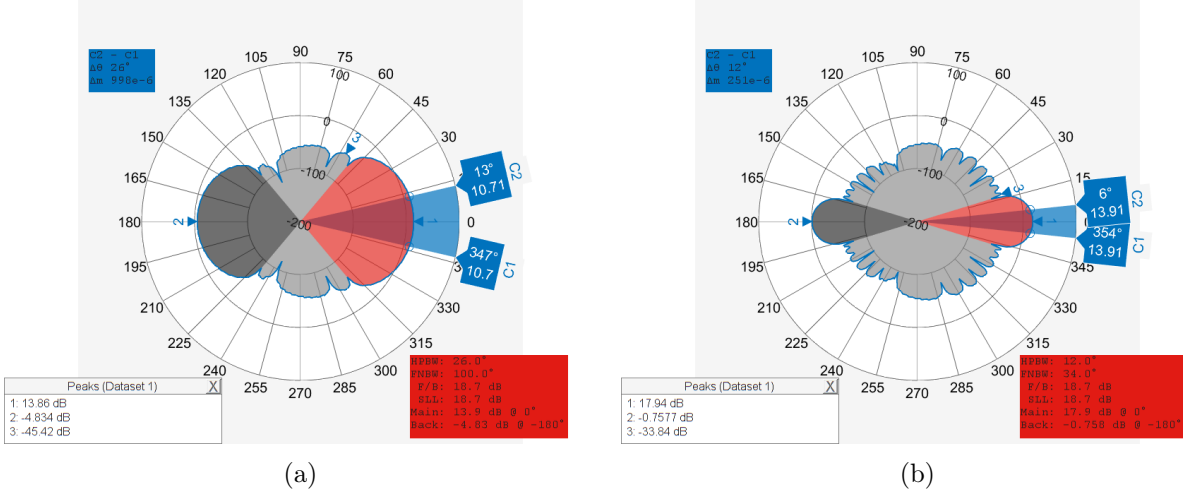


Figure 2.26: Polar radiation pattern at 5 GHz for Chebyshev Array of Patch Microstrip Antennas: (a) $N = 5$, (b) $N = 15$

2.6.2 Results

Fig. 2.27 shows the trend of the Main Lobe Magnitude as a function of the number of N antenna elements from which the Chebyshev array is composed. As expected, as N increases, ranging from 3 to 20, the analyzed value tends to increase from about 12.5 dB , for $N = 3$, to about 19.2 dB , for $N = 20$. The array, therefore, turns out to be more directive with a greater gain in the direction of the main lobe, meeting the objectives of a Chebyshev array.

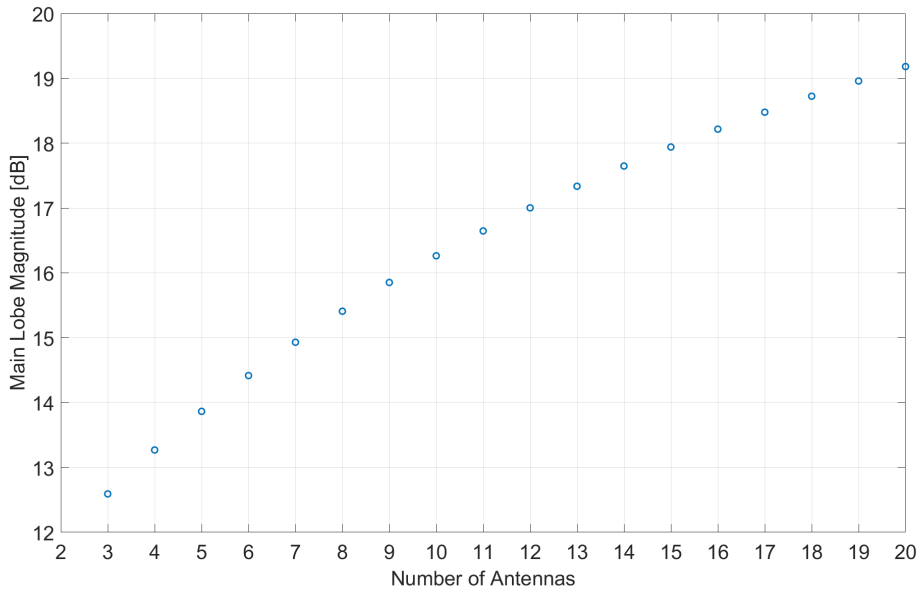


Figure 2.27: Main Lobe Magnitude as a function of number of antenna elements N for Chebyshev Array of Patch Microstrip Antennas at 5 GHz

The graph in Fig. 2.28 shows how the HPBW varies as the number of antenna elements increases. It starts from an angular resolution of about 36° , to a narrowing to 8° . This trend is consistent with that described for the magnitude of the main lobe, confirming the improved directivity of the beam.

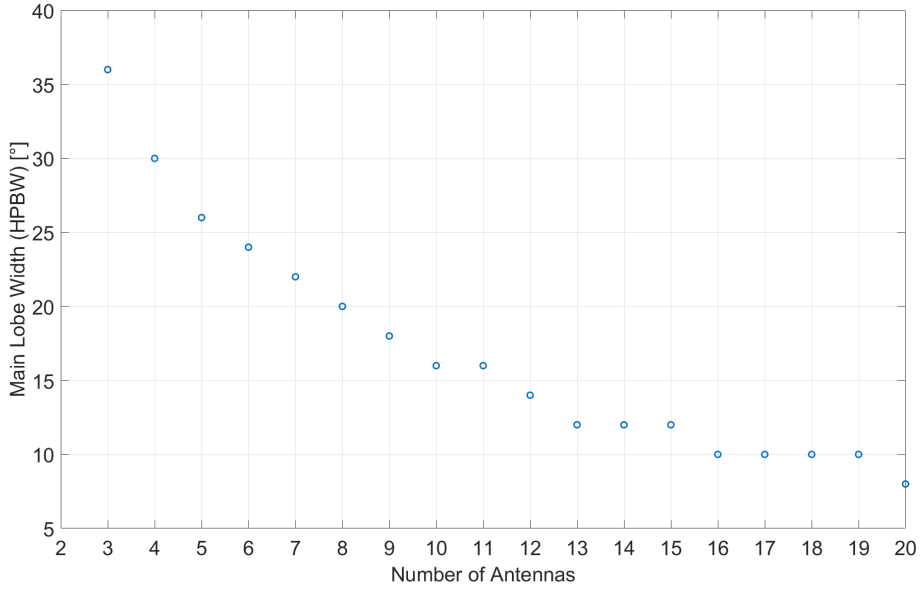


Figure 2.28: Main Lobe Width as a function of number of antenna elements N for Chebyshev Array of Patch Microstrip Antennas at 5 GHz

The trend of Main Lobe Direction shown in Fig. 2.29 is constant as in the other analyses performed without changing the phase shift. By varying the number of antennas, there will therefore be no beamsteering and the main lobe will always point in the broadside direction as expected.

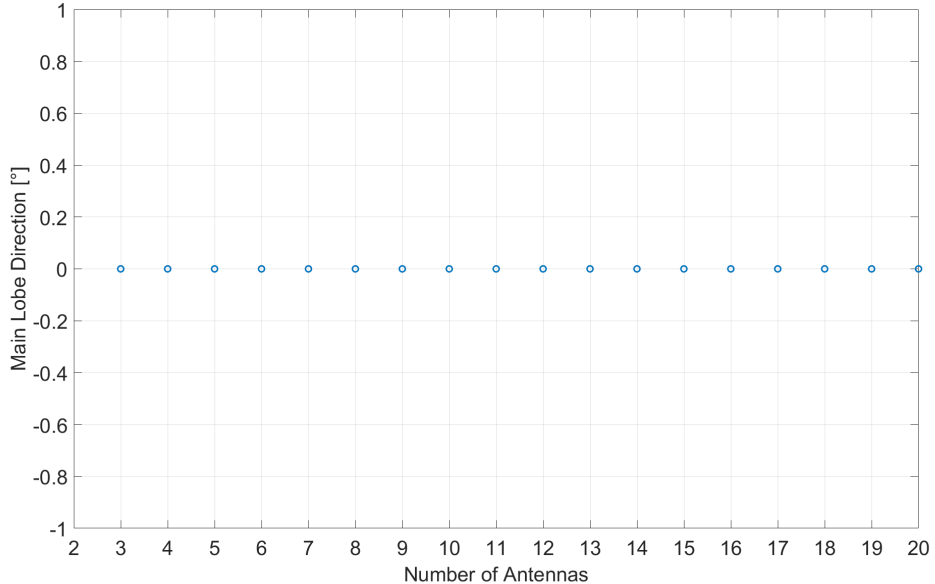


Figure 2.29: Main Lobe Direction as a function of number of antenna elements N for Chebyshev Array of Patch Microstrip Antennas at 5 GHz

In Fig. 2.30, an increasing trend for Side Lobe Magnitude can be observed as the number of microstrip patches considered increases. Regarding the $N = 3$ antennas case, we start with a magnitude of -54 dB going up to about -36 dB with 20 antennas. This behavior is due to the higher directivity of the main lobe, and thus a higher power distribution in the side lobes.

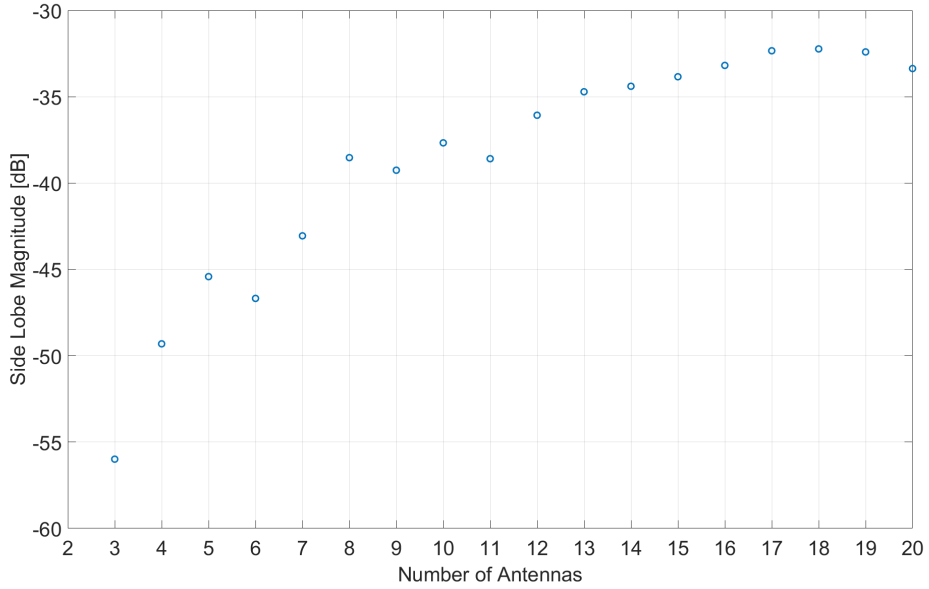


Figure 2.30: Side Lobe Magnitude as a function of number of antenna elements N for Chebyshev Array of Patch Microstrip Antennas at 5 GHz

To confirm the trend of side lobe magnitude, we evaluate in Fig. 2.31 the SLL.

A single microstrip patch has a broad main lobe and a back lobe of reduced intensity. When making a Chebyshev array with a limited number of elements, the total pattern may be irregular because some side lobes in the array are in directions where the element factor has a very low value, generating undesirable variations in the amplitude of the side lobes. For example, for $N = 3$ we have 69 dB, compared to the desired reference value of 50 dB.

By increasing the number of antennas in the array, the main lobe and side lobes all concentrate in angular regions where the magnitude of the single element main lobe is more uniform. In this way, the resulting pattern is less influenced by the variation of the envelope and the SLL is closer to that predicted by the array synthesis. In fact, starting at $N = 13$, we confirm the consideration just made, with an SLL that is almost at 50 dB.

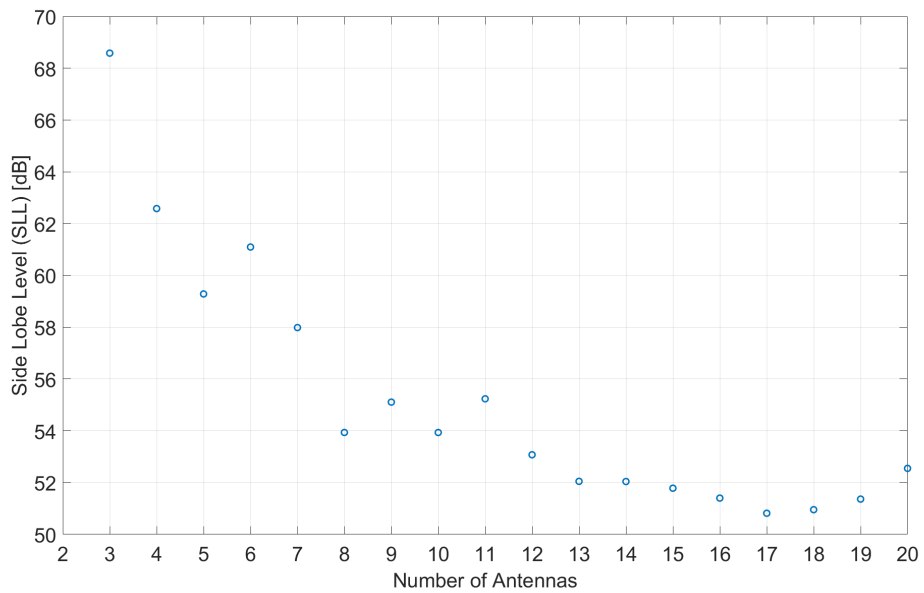


Figure 2.31: Side Lobe Level as a function of number of antenna elements N for Chebyshev Array of Patch Microstrip Antennas at 5 GHz

2.7 Comparison

This project investigated the performance of various configuration of antenna arrays, including ULA, Binomial, and Chebyshev arrays. The analysis highlighted how changes in the number of antenna elements N and the phase shift between adjacent elements impact critical array parameters, such as main lobe magnitude, width, direction and side lobe magnitude and SLL. To compare the three configurations, the arrays were examined across different sizes, with N values ranging from 3 to 20.

Since the effect of the current phase shift has been only explored for the ULA, and its effects are about the direction, we will mainly compare the other figures of merit.

In Fig. 2.32, we compare the Main Lobe Magnitude for the ULA, Binomial and Chebyshev array configurations, varying the number of N elements. The analysis reveals a clear trade-off between main lobe magnitude, main lobe width and side lobe control. As N increases, all configurations show an increase in main lobe magnitude.

The uniformly fed **ULA** configuration exhibits the highest main lobe magnitude due to the higher concentration of energy in the main lobe, with a maximum of 21 dB. However, this choice results in significant side lobes making it unsuitable in interference-sensitive contexts.

The **Binomial array**, designed to suppress side lobes almost completely, sacrifices much of the main lobe magnitude and widens the beamwidth, limiting so the precision of the beam. As we see, it turns out to be the configuration in which this parameter has the lowest values in comparison with the other configurations.

The **Chebyshev array**, on the other hand, does not excessively degrade the main lobe magnitude, aiming at precise control of the SLL, rather than cancellation of the side lobes. Thus, as far as main lobe magnitude is concerned, the Chebyshev array turns out to be an intermediate solution between the three proposed.

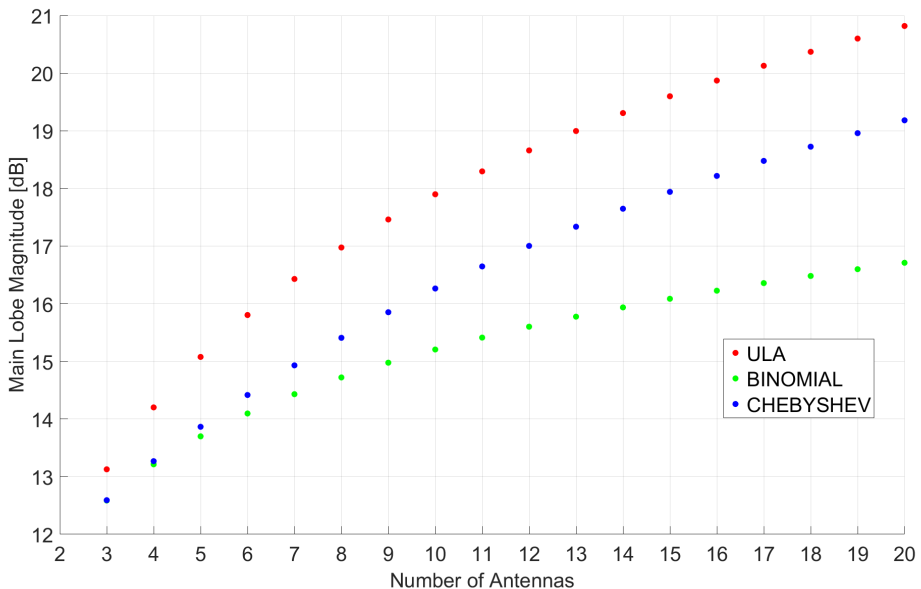


Figure 2.32: Main Lobe Magnitude as a function of number of antenna elements N for ULA, Binomial and Chebyshev array of Patch Microstrip Antennas at 5 GHz

The comparison of the Main Lobe Width among the three configurations is shown in Fig. 2.33.

It is observed that as N increases, the HPBW narrows progressively for all configurations, reflecting the improvement in directivity due to higher element density.

The **ULA** configuration, due to uniform tapering, has the narrowest main lobe under all conditions, due to the constructive interference achieved between elements. However, this precise focus is accompanied by high secondary lobes.

In contrast, the **Binomial array**, designed to cancel side lobes by tapering the amplitudes of the currents feeding the antenna elements, exhibits the widest HPBW, as the progressive reduction of the weights at the extremes increases the width of the beam, sacrificing directivity in favor of the absence of side lobes.

The **Chebyshev** configuration, which is optimized to control the level of side lobes to a specific value, again falls somewhere in between: the HPBW is narrower than the Binomial but slightly wider than the ULA. This balance comes from equi-ripple synthesis, which redistributes energy to limit side lobes without unduly compromising directivity.

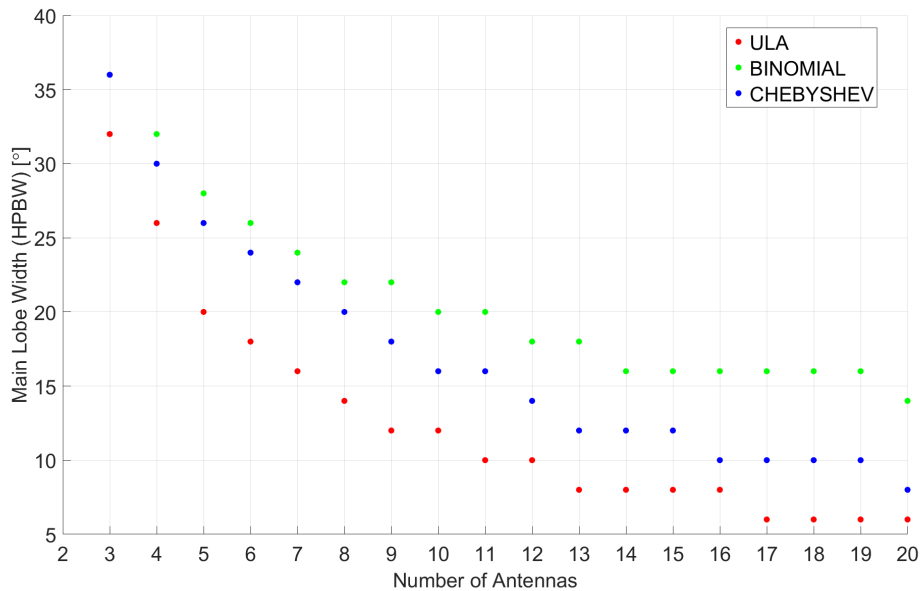


Figure 2.33: Main Lobe Width as a function of number of antenna elements N for ULA, Binomial and Chebyshev array configuration of Patch Microstrip Antennas at 5 GHz

The direction of the main lobe remains constant for all three configurations, as expected under broadside operating conditions. Since no progressive phase shift is applied between elements, the main lobe is always oriented along the x -axis direction, consistent with the physical alignment of the array along the y -axis. This geometry ensures that, in the absence of beam steering, the maximum radiation remains perpendicular to the axis of alignment of the elements, regardless of the amplitude distribution adopted.

The introduction of a progressive phase shift between adjacent elements allows the beam to be steered in different directions. In a ULA, the application of a linear phase shift allows precise orientation of the beam. For a binomial array, steering is possible,

but it modifies the original amplitude distribution, risking the reemergence of secondary lobes previously suppressed due to the binomial taper perturbation. In a Chebyshev array, beam steering can be accomplished, but it alters the uniform levels of the side lobes, compromising the typical behavior of this configuration. In fact, to keep the side lobes constant, the amplitude weights must be recalculated for each steering angle, increasing the design complexity compared to a ULA [3].

Fig. 2.34 compares the Side Lobe Magnitude as the number of N elements varies.

The **ULA** configuration has higher side lobes, with quite high values that are around -13 dB , because the energy concentration in the main lobe is not balanced with any suppression of the side lobes.

In contrast, the **Binomial array**, thanks to a progressive taper that almost completely cancels the side lobes, achieves extremely low levels of side lobes, theoretically zero for ideal distributions, especially if we consider a larger number of antennas.

The **Chebyshev** configuration, designed to maintain a constant and controlled level of side lobes, in our case 50 dB , offers an optimal compromise: side lobes are significantly lower than in the ULA, but higher than in the Binomial array, while maintaining a sufficiently high magnitude and a fairly narrow main lobe.

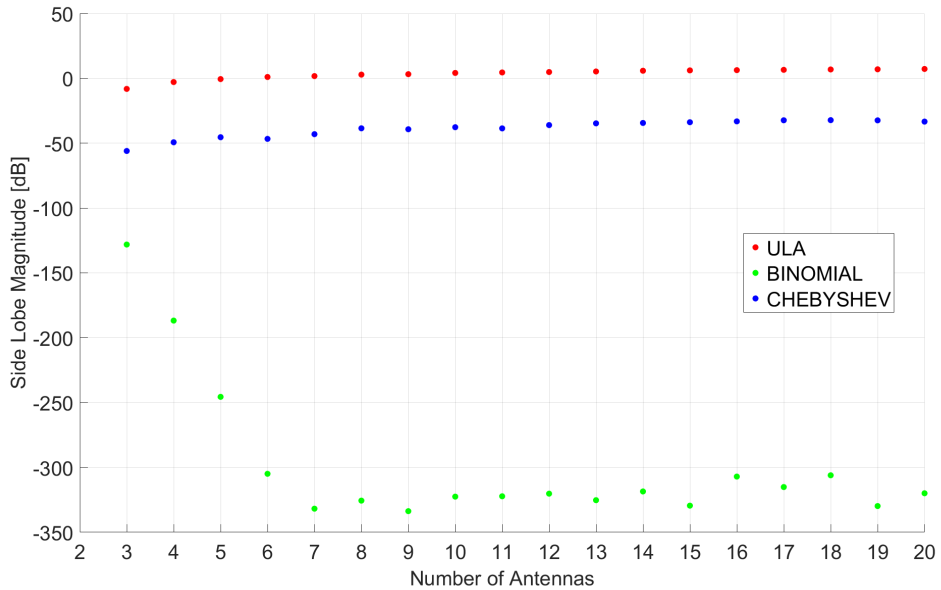


Figure 2.34: Side Lobe Magnitude as a function of number of antenna elements N for ULA, Binomial and Chebyshev array of Patch Microstrip Antennas at 5 GHz

Finally, Fig. 2.35 compares the SLL as the number of N antenna elements varies. Since higher values indicate better suppression of side lobes, the analysis reveals distinct behaviors.

The **Binomial** configuration achieves the highest SLL values, confirming its effectiveness in minimizing side lobes. This approach, however, as seen above, results in a larger main lobe and reduced magnitude .

The **Chebyshev** configuration, optimized to maintain a constant SLL, is positioned in an intermediate zone, balancing suppression of side lobes and maintenance of directivity.

The **ULA**, with uniform weights, shows the lowest SLL values, indicative of the presence of pronounced side lobes, typical of arrays that do not have ad-hoc tapering for their removal.

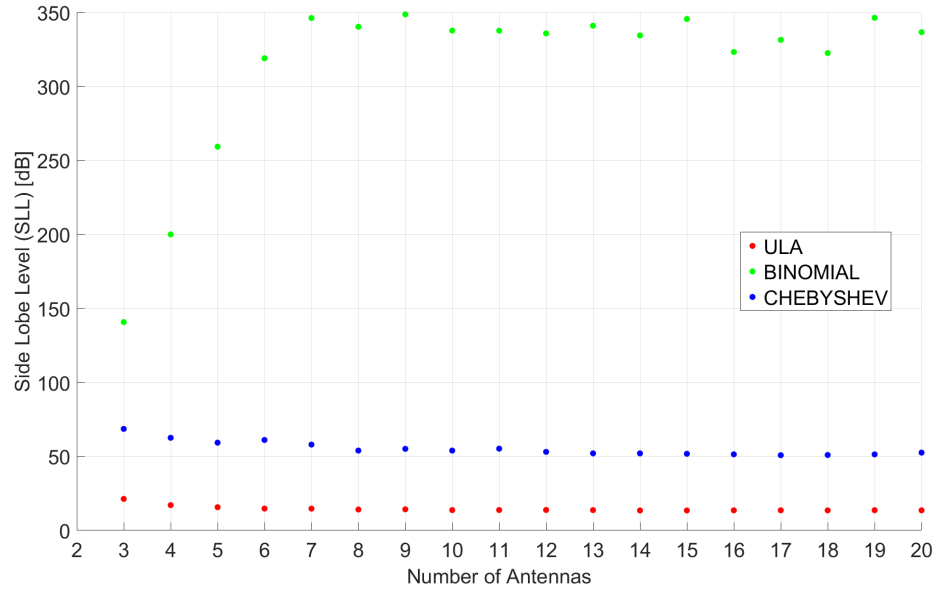


Figure 2.35: Side Lobe Level as a function of number of antenna elements N for ULA, Binomial and Chebyshev array of Patch Microstrip Antennas at 5 GHz

2.8 Conclusion

Comparative analysis of the ULA, Binomial, and Chebyshev array configurations reveals the need for trade-offs between directivity, secondary lobe control, and design complexity. The ULA configuration, characterized by uniform power supply, provides the highest main-lobe magnitude and minimum lobe width, optimizing directivity and simplicity of implementation, but at the expense of pronounced secondary lobes, which limits its use in interference-sensitive contexts. The Binomial array, designed to cancel side lobes, achieves the most effective secondary lobe suppression, ideal for applications requiring spectral purity, but sacrifices directivity with a wider main lobe and reduced magnitude. The Chebyshev configuration, on the other hand, represents the optimal compromise, maintaining a controlled SLL and acceptable directivity, thanks to equi-ripple synthesis that balances energy in the main lobe and suppression of side lobes, while requiring a more complex design.

Under broadside conditions, thus without beamsteering, all three configurations keep the main lobe oriented along the x axis, consistent with the physical alignment along y . However, the absence of progressive phase shifts highlights how the choice of array depends on application goals: the ULA is preferred for maximizing gain, the Binomial for eliminating interference, and the Chebyshev for scenarios requiring a balance between performance and lobe control. The simulated data, displayed in the figures, confirm that the Chebyshev is positioned as a versatile solution, while the ULA and Binomial remain specialized options, each with their respective downsides analyzed.

The comparison offers insights for future developments, starting with beam steering analysis for the Binomial and Chebyshev arrays, exploring how they respond to progressive phase shifts, with focus on parameter optimization.

Another development would involve the integration of real and non-ideal elements: for the analyses conducted, a microstrip patch of totally reflective material (PEC) was considered without taking into account the effects of a substrate composed of a material used in real contexts.

Bibliography

- [1] Kai-Fong Lee and Kin-Fai Tong, “Microstrip patch antennas—basic characteristics and some recent advances,” vol. 100, no. 7, pp. 2169–2180.
- [2] Y. Liu, L.-M. Si, M. Wei, P. Yan, P. Yang, H. Lu, C. Zheng, Y. Yuan, J. Mou, X. Lv, and H. Sun, “Some recent developments of microstrip antenna,” vol. 2012, pp. 1–10.
- [3] C. A. Balanis, *Antenna theory: analysis and design*. John wiley & sons, 2016.